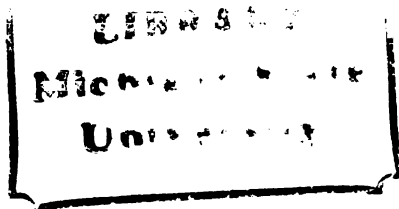




THESIS



This is to certify that the

thesis entitled

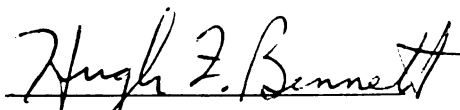
AZIMUTHAL VELOCITY-DEPTH DISTRIBUTION OF SEISMIC  
SHEAR AND COMPRESSIONAL WAVES IN THE ROSS ICE  
SHELF, 18 km EAST OF MINNA BLUFF, AND 96 km  
SSE OF McMURDO STATION, ANTARCTICA

presented by

James B. Wanslow

has been accepted towards fulfillment  
of the requirements for

M. S. degree in Geology

  
Major professor

Date 20 May 1981



OVERDUE FINES:

25¢ per day per item

RETURNING LIBRARY MATERIALS:

Place in book return to remove  
charge from circulation records

AZIMUTHAL VELOCITY-DEPTH DISTRIBUTION OF SEISMIC  
SHEAR AND COMPRESSIONAL WAVES IN THE ROSS ICE  
SHELF, 18 km EAST OF MINNA BLUFF, AND 96 km  
SSE OF McMurdo Station, Antarctica

By

James B. Wanslow

A THESIS

Submitted to  
Michigan State University  
in partial fulfillment of the requirements  
for the degree of

MASTER OF SCIENCE

Department of Geology

1981



6/18/11

## ABSTRACT

### AZIMUTHAL VELOCITY-DEPTH DISTRIBUTION OF SEISMIC SHEAR AND COMPRESSIONAL WAVES IN THE ROSS ICE SHELF, 18 km EAST OF MINNA BLUFF, AND 96 km SSE OF McMURDO STATION, ANTARCTICA

By

James B. Wanslow

This study was undertaken to determine the azimuthal seismic velocity-depth distribution in an area of known high shear stress. It was assumed that the effects of the shear stress field would be reflected in the azimuthal velocity-depth distribution because of the known response of ice fabric to shear stress. A site 18 km east of the Minna Bluff peninsula and 96 km SSE of McMurdo Station, Antarctica, was selected for the study due to the nature of the shear stress field in this region.

Seismic data collected in 8 directions using a radial refraction array was analyzed to produce velocity-depth profiles. The distribution of SH-wave velocities was bimodal and centrosymmetric, with one maximum velocity set averaging  $2056 \text{ ms}^{-1} \pm 24 \text{ ms}^{-1}$ , and the other  $1830 \text{ ms}^{-1} \pm 18 \text{ ms}^{-1}$ . P-wave velocities displayed no centro-symmetry, and exhibited an average maximum velocity of  $3671 \text{ ms}^{-1} \pm 15 \text{ ms}^{-1}$ . The SH-wave results were attributed to a strong east-west ice crystal c-axis orientation with vertical basal planes below 37 m depth. The low P-wave velocity maximum was attributed primarily to fracturing. The importance of shear waves for velocity anisotropy studies was thus indicated.

This work is dedicated to  
my wife Linda,  
whose assistance and tolerance  
helped make it possible.

## ACKNOWLEDGMENTS

I would like to express my gratitude to Dr. Hugh Bennett, whose guidance and instruction made this thesis possible. Special recognition for typing assistance and moral support is also due my sister-in-law, Nancy Payne, and, most especially, my wife, Linda Wanslow, without whom this work might never have been completed. Lastly, I must acknowledge assistance and support of a different kind provided to me over many years by my mother, Lucille Wanslow, to whom I will always owe a large debt of gratitude.

## TABLE OF CONTENTS

Introduction.....	1
Previous Seismic Work on the Ross Ice Shelf.....	1
Pertinent Ice Petrofabric Research.....	2
Pertinent Ultrasonic Research.....	3
Purpose.....	4
Location of the Study Area.....	4
Pertinent Glaciological Aspects of the Ross Ice Shelf..	9
Surface Features.....	9
Source Areas, Flow Direction, and Ice Thickness...	10
Stratification.....	14
Effect of Glaciological Parameters on Seismic Wave Propagation.....	17
Field Procedures.....	21
Field Season and Personnel.....	21
Description of Seismic Array, Equipment, and Procedures.....	21
Distance and Time Measurement.....	23
Data Reduction: Time-Distance Curves.....	25
Introduction.....	25
Discussion of Time-Distance Curves.....	25
Analysis and Interpretation.....	39
Introduction.....	39

Velocity Determination and Error Analysis.....	39
Velocity-Depth Profiles.....	45
Interpretation of Velocity-Depth Profiles:	
Developement of Model.....	57
Velocity Increase to 37 m Depth:	
Densification.....	57
Velocity Increase 37 m to 70 m Depth:	
Crystal Fabric.....	59
Heterogeniety in the Near Surface.....	61
P-Wave Velocities Affected by Fracturing.....	62
Proposed Model for the Minna Bluff Study Area.....	65
Comparison of Velocity-Depth Profiles near Minna	
Bluff with Other Studies.....	65
Importance of Shear Waves in Seismic Anisotropy	
Studies.....	67
Appendix A: Transverse Isotropy.....	70
Appendix B: Derivation of Weichert-Herglotz-Bateman	
Integral.....	75
Appendix C: Seismic Event Recognition and Arrival Time	
Determination.....	83
Appendix D: SH-Wave Time-Distance Data.....	85
Appendix E: Seismic Velocities and WHB Depths.....	91
Bibliography.....	93

## LIST OF TABLES

I	SH-Waves: Regression Lines and Maximum Velocities	37
II	P-Waves: Regression Lines and Maximum Velocities.	37
III	Error Analysis.....	43
D-I	SH-Wave Time-Distance Data.....	85
D-II	P-Wave Time-Distance Data.....	88
E-I	Seismic Velocities and WHB Depths.....	91

## LIST OF FIGURES

1.	Ross Ice Shelf, Minna Bluff Vicinity.....	6
2.	ERTS Photo, Minna Bluff Area.....	8
3.	Crevasse Fields of the Ross Ice Shelf.....	11
4.	Thickness of the Ross Ice Shelf.....	13
5.	Velocity field of ice movement, Ross Ice Shelf...	16
6.	Density profiles at Byrd Station, Little America V, and Ellsworth.....	18
7.	Temperature profile at Byrd and Little America V.	18
8.	T-X curve, SH waves Set A: 000-090 directions....	27
9.	T-X curve, SH waves Set B: 045-135 directions....	28
10-A.	T-X curve, non-linear part, SH-000-D.....	29
10-B.	T-X curve, non-linear part, SH-000-R.....	29
10-C.	T-X curve, non-linear part, SH-045-D.....	30
10-D.	T-X curve, non-linear part, SH-045-R.....	30
10-E.	T-X curve, non-linear part, SH-090-D.....	31
10-F.	T-X curve, non-linear part, SH-090-R.....	31
10-G.	T-X curve, non-linear part, SH-135-D.....	32
10-H.	T-X curve, non-linear part, SH-135-R.....	32
11-A.	P-Wave T-X curve, 000 and 090 directions.....	33
11-B.	P-Wave T-X curve, 045 and 135 directions.....	34
12.	Best Fit Curves, Shear Wave Set A and B.....	35
13-A.	Depth vs Error, SH-Waves.....	44
13-B.	Depth vs Error, P-Waves.....	44



14-A. Velocity-Depth Profile: Line SH-000-D.....	47
14-B. Velocity-Depth Profile: Line SH-000-D.....	47
14-C. Velocity-Depth Profile: Line SH-045-D.....	48
14-D. Velocity-Depth Profile: Line SH-045-R.....	48
14-E. Velocity-Depth Profile: Line SH-090-D.....	49
14-F. Velocity-Depth Profile: Line SH-090-R.....	49
14-G. Velocity-Depth Profile: Line SH-135-D.....	50
14-H. Velocity-Depth Profile: Line SH-135-R.....	50
15-A. Velocity-Depth Profile: Line P-000-D.....	51
15-B. Velocity-Depth Profile: Line P-000-R.....	51
15-C. Velocity-Depth Profile: Line P-045-D.....	52
15-D. Velocity-Depth Profile: Line P-045-R.....	52
15-E. Velocity-Depth Profile: Line P-090-D.....	53
15-F. Velocity-Depth Profile: Line P-090-R.....	53
15-G. Velocity-Depth Profile: Line P-135-D.....	54
15-H. Velocity-Depth Profile: Line P-135-R.....	54
16. Velocity-Depth Profile: SH-Waves Set A.....	55
17. Velocity-Depth Profile: SH-Waves Set B.....	56
18. Density vs P-wave velocity, linear plot, at Byrd Station.....	58
19. P-wave and S-wave velocities and densities vs depth at Byrd Station.....	59
20. ....	59
21. Velocity-Depth Profiles at Byrd, at Little America V, and at Ellsworth.....	66
22. Ross Ice Shelf P and SH-wave Velocity-Depth Profiles.....	68

23.	.....	75
24.	.....	77
25.	.....	78
26.	.....	78
27.	.....	79
28.	SH-Wave identification; sample of corresponding overlaid traces.....	84

## I. INTRODUCTION

### PREVIOUS SEISMIC WORK ON THE ROSS ICE SHELF

The first intensive seismic reconnaissance program covering the entire Ross Ice Shelf was performed during the years 1957 through 1960 as a part of the United States IGY activities in Antarctica. Three traverses were carried out: the Ross Ice Shelf Traverse of 1957-1958, the Victoria Land Traverse of 1958-1959, and the Discovery Deep Traverse of 1960 (Crary, et al., 1960). Seismic reflection and refraction surveys were carried out at stations along the traverse routes in conjunction with other glaciological studies. Goals of the seismic program included determination of ice thickness, mapping of water depth beneath the ice shelf, and measurement of seismic velocities within the ice. Results of the surveys included maps of ice thickness and water depth for the shelf as a whole. Seismic velocity was found to increase as an approximately logarithmic function of depth, with maximum velocity attained at a depth of 60 to 80 meters.

The velocity-depth profile at Little America V on the Ross Ice Shelf was constructed by seismic refraction work in conjunction with the deep core drilling project of 1958-1959 (Thiel and Ostenso, 1961). Comparison of the velocity-depth profile with the density-depth profile produced by the core drilling project indicated that to a first approximation the increase of velocity with depth reflected the increase of density with depth. Maximum compressional wave velocity was reached at 80 to 85 meters depth, as estimated from the

refraction survey. This compares well with the depth of 85 to 110 meters determined for maximum velocity from seismic logging of the deep drill hole. Maximum P-wave velocity was measured as  $3839 \text{ ms}^{-1}$  and maximum S-wave velocity as  $1978 \text{ ms}^{-1}$ .

#### PERTINENT ICE PETROFABRIC RESEARCH

Crystal fabric studies of temperate and polar glaciers have demonstrated that the c-axes of ice crystals tend to be aligned perpendicular to the foliation plane (Rigsby, 1960; Taylor, 1963; others). Rigsby has further demonstrated that the alignment is strongest with high shear stress. Recrystallization during deformation with resulting c-axis alignment normal to applied shear stress has been observed by Rigsby during study of ice stressed under controlled laboratory conditions. Plastic deformation of ice is accomplished by translation gliding on the basal plane (Kamb, 1961). Glide direction and direction of shear stress correspond closely. Petrofabric studies of the deep drill core at Little America V have disclosed an increasing preferred orientation of c-axes with depth (Ragle, et al., 1960). In a study of ice fabrics from the Thule area in Greenland, Rigsby concluded that ice crystals in polar glaciers tend to be oriented with the basal glide plane parallel to the shear plane (Rigsby, 1955).

PERTINENT ULTRASONIC RESEARCH

Laboratory studies of ultrasonic wave propagation in single ice crystals have demonstrated the dependence of velocity on propagation direction in a transversely isotropic manner (Appendix A). A difference of about 4% between P-wave velocity in the c- and a-axis directions has been observed, with a maximum difference of nearly 7% between propagation in the c-axis direction and at 52° to the c-axis (Bennett, 1968). In a study of the effects of conic crystal distributions, with a vertical axis of symmetry, a difference of < 2% in P-wave velocity between the vertical and horizontal directions was found for c-axis distributions inclined at > 30° to the vertical (Bennett, 1972). Horizontal SH and SV-wave velocities were found to differ by at least 2% even for very slight preferred orientations. This, in conjunction with the ice petrofabric results cited above, implies that detection of preferred c-axis orientation in polycrystalline ice may be possible by determining the distribution of velocity with direction. If a preferred orientation is indeed present, then a directional dependency may be observable. It should be noted that velocity variations of a transversely isotropic nature may result from layering (Postma, 1955). Foliation often observed in glacier ice (Rigsby, 1960; Shumskii, 1964; Embledon and King, 1968), consisting of alternating layers of bubbly and clear ice or of microfracturing, which are believed to result from flow deformation (Embledon and King, 1968), would represent such a layering. Postma (1955) has

shown that in such a case the slow direction of P-wave propagation would be normal to the layering.

#### PURPOSE

The purpose of this study is to determine the distribution of seismic velocity with depth and azimuth in an area of known high shear stress. It is assumed that the velocity distribution should be related to the direction of shear stress because of the response of ice fabrics to shear stress as discussed above. Thus, if the aggregate c-axis orientation is as indicated, the pattern of the seismic velocity distribution should be predictable. Therefore, determination of the velocity-depth profile as a function of azimuth should permit analysis of the effects of the stress field on the ice fabric.


#### LOCATION OF THE STUDY AREA

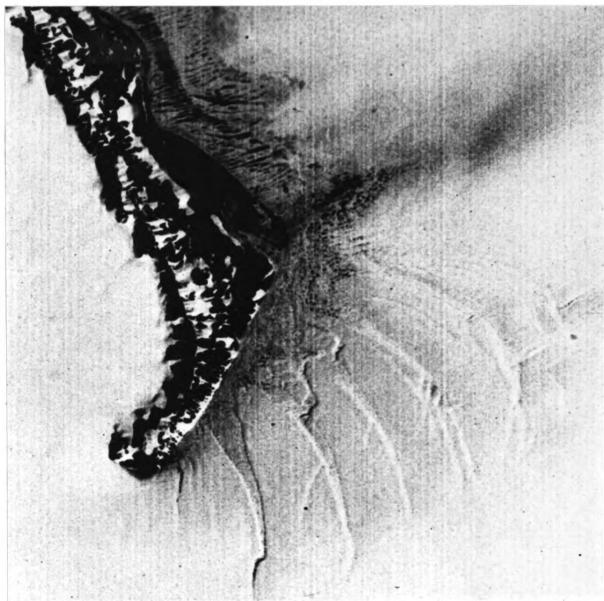
The study area is located on the Ross Ice Shelf, 18 km east of Minna Bluff and about 96 km SSE of McMurdo Station, Antarctica (Figures 1 and 2). The gross ice movement in the area is to the north. The ice movement is retarded by Minna Bluff, however, resulting in a zone of high strain rates in the shear stress field imposed by the movement past Minna Bluff (Crary, et al. 1962).

Figure 1. Ross Ice Shelf, Minna Bluff Vicinity. Study area  
indicated by ● ←





Figure 2. ERTS Photo, Minna Bluff Area. Study area indicated by ● 



## II. PERTINENT GLACIOLOGICAL ASPECTS OF THE ROSS ICE SHELF

### SURFACE FEATURES

Glaciological work of the IGY traverses listed in Chapter 1 included mapping of snow accumulation rates and surface density (Crary, et al., 1962). Snow accumulation studies employing surface stakes, pit studies, and drill core analysis indicated an average annual accumulation rate of 20 centimeters water equivalent per unit area for the entire Ross Ice Shelf. For most areas annual values ranged from 17 to 24 centimeters water equivalent per unit area (Crary, et al., 1962; Zumberge, et al., 1960). In the vicinity of Minna Bluff estimated annual accumulation ranged from 17.6 to 23.5 centimeters water equivalent per unit area. Bulk density measurements of the top two meters of the shelf indicated a range of 0.33 to 0.42 gm cm<sup>-3</sup> for the entire ice shelf. A range of 0.40 to 0.41 gm cm<sup>-3</sup> was observed in the vicinity of Minna Bluff.

Sastrugi may be defined as a series of wavelike or domelike ridges formed by wind action. Well-developed sastrugi with strong north-south orientation was observed in the study area (H. Bennett, personal communication). Mean peak to trough amplitude of the sastrugi was estimated to be 0.5 meters.

Crevasses and fractures result from internal stresses exceeding certain parameters of the ice strength (Zumberge, et al., 1960). Thus, areas of high strain rates are implied by the locations of crevasse fields, as indicated

schematically in Figure 3. Note especially the crevasse field east of Minna Bluff indicated in Figure 3 and shown by ERTS photography in Figure 2. In crevasse fields, fractures ranging in width from several meters down to a few millimeters may be observable. In the case of extremely narrow fractures, it is not possible to determine the nature of the fracture at depth by visual observation alone. An attempt was made on the basis of preliminary aerial and ground reconnaissance to locate the study area completely outside the crevasse field adjacent to Minna Bluff. However, more detailed observation, during the course of the field work, revealed the presence of several very narrow but long fractures at the surface in the vicinity of the study area (H. Bennett, personal communication).

#### SOURCE AREAS, FLOW DIRECTIONS, AND ICE THICKNESS

The major sources of the Ross Ice Shelf are the Marie Byrd Land Ice Sheet, the glaciers of the Transantarctic Mountains, and snow accumulation directly on the ice shelf (Crary, et al., 1962). The largest contribution is from Marie Byrd Land, as clearly seen from the isopachs of Figure 4. The glacial ice streams from the Transantarctic Mountains, forming the second largest ice source, are clearly discernable in the same figure. Snow accumulation on the ice shelf, discussed above, was concluded by Crary (1962) to be the third largest source. In cores from the deep drilling project at Little America V, annual strata were discernable to at least 50 m depth (Ragle, et al., 1960). The stratification was

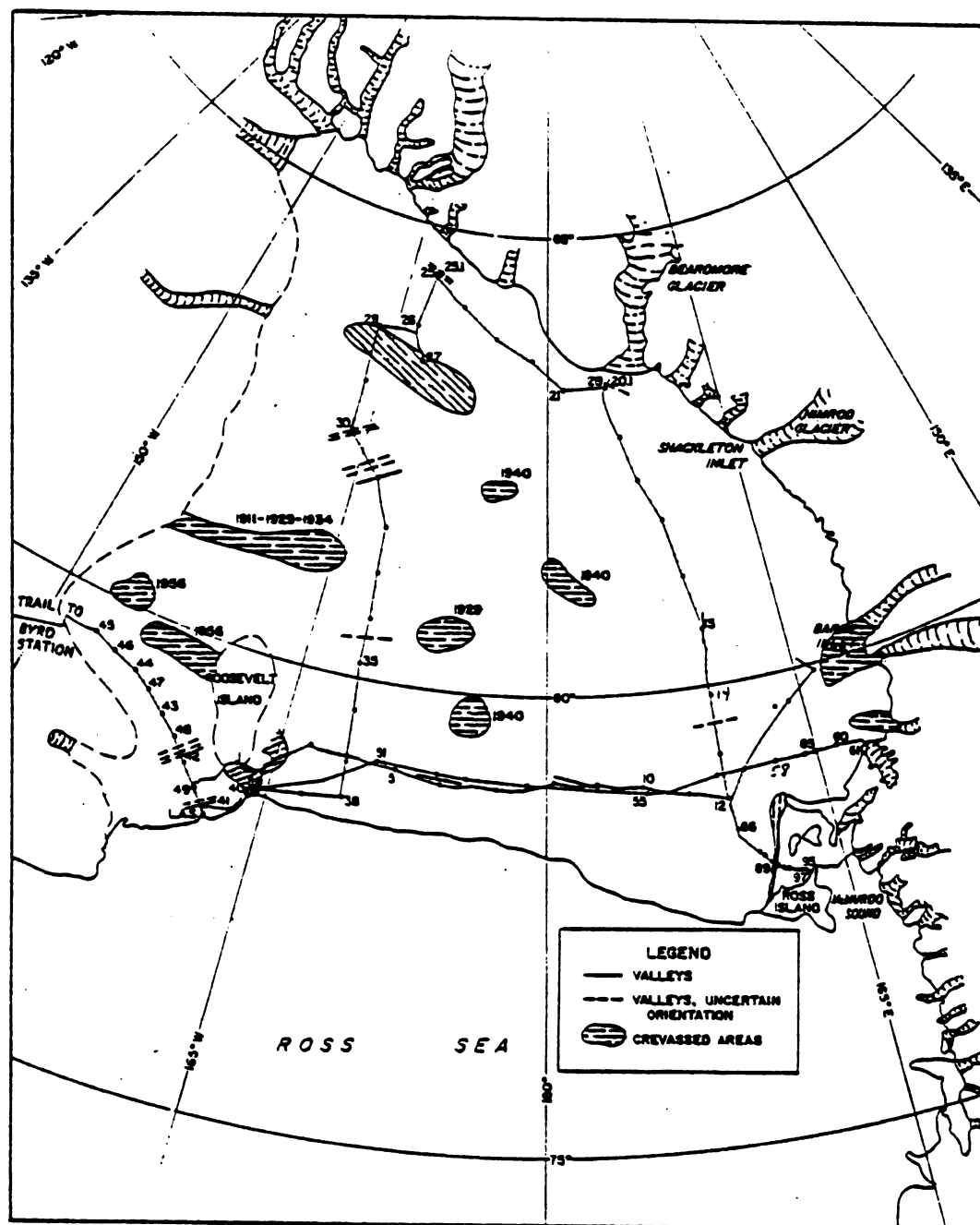


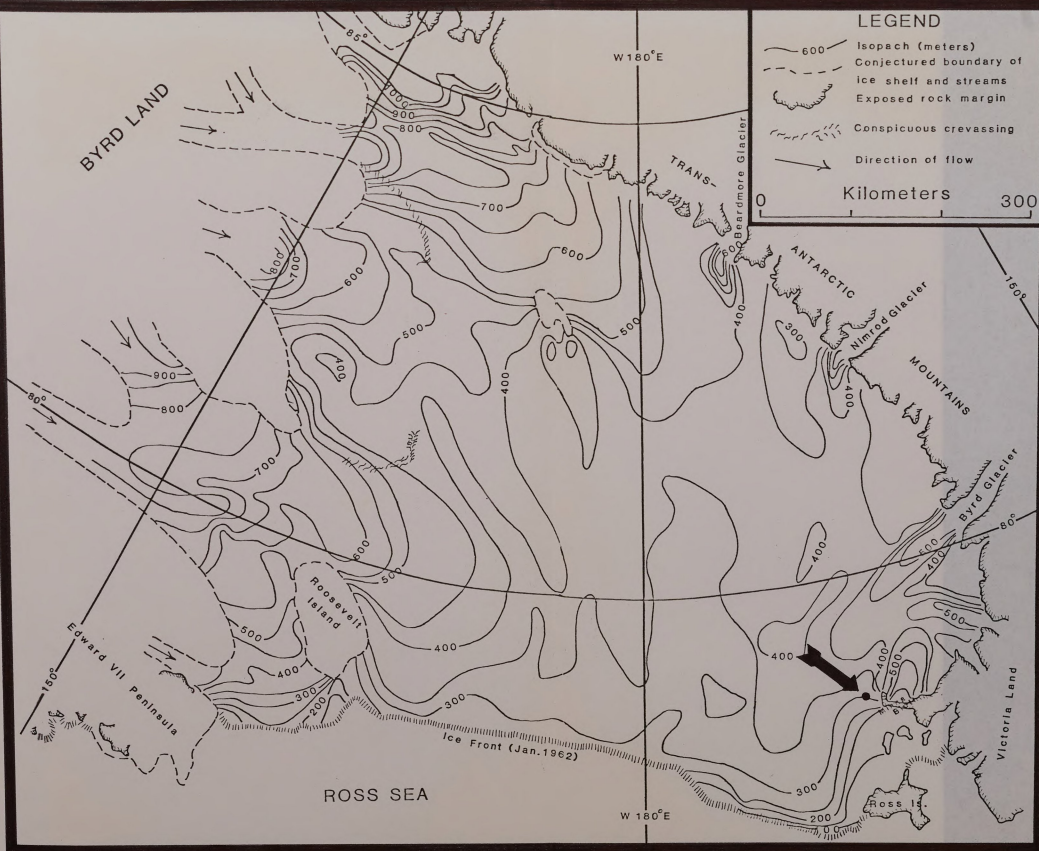
Figure 3. Crevasse fields of the Ross Ice Shelf. (From Crary, et al., 1962)

Figure 4. Thickness of the Ross Ice Shelf. (After Robin,  
1975)

# LEGEND

- Isopach (meters)
- Conjectured boundary of ice shelf and streams
- Exposed rock margin
- Conspicuous crevassing
- Direction of flow

0 Kilometers 300



attributed by Ragle, et al., to accumulation on the ice shelf, although it should be noted that annual strata are also recognizable in the ice sheet at Byrd Station (Gow, 1961). Ragle, et al., concluded that, due to melting at the bottom of the ice shelf, ice developed from annual snow accumulation may form a major fraction of the total shelf thickness near the terminus. It should be noted, however, that the whole question of melting at the base of the shelf is very controversial.

Ice flow directions have been determined by observations of stake movements, mapping of thickness trends and visible flow lines, and surface leveling (Dorrer, et al., 1969; Stuart and Bull, 1963; Crary, et al., 1962; MacDonald and Hatherton, 1961). Recently, Robin (1975) has compiled a comprehensive map of velocity vectors and flow directions for the entire ice shelf (Figure 5). Note especially in Figure 5 the flow direction near Minna Bluff.

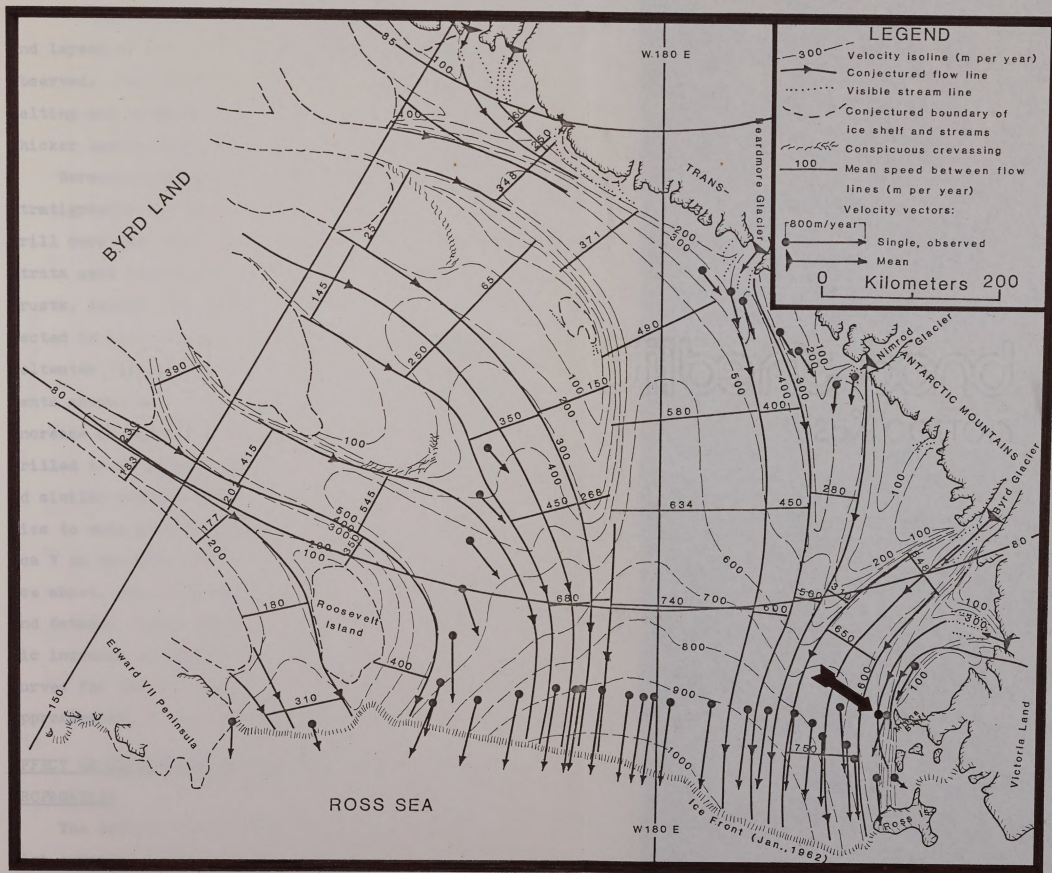
Thickness of the Ross Ice Shelf has recently been mapped by airborne radio sounding techniques (Robin, 1975) (Figure 4). Note in Figure 4 the damming effect of Minna Bluff as evidenced by the great ice thickness immediately behind and against it, and the rapid thinning adjacent to the east.

#### STRATIFICATION

During the traverses of 1959-1960, snow pit studies to 3 meters depth revealed annual strata readily discernable by textural variations (Crary, et al., 1962). Small ice lenses, probably formed by refreezing of meltwater, as well as crusts



Figure 5. Velocity field of ice movement, Ross Ice Shelf.  
(After Robin, 1975)



and layers of ice up to several centimeters thick were also observed. The crusts and layers were attributed to surface melting and refreezing followed by burial. Some of the thicker layers were correlatable over a relatively wide area.

Borehole studies performed during the IGY included stratigraphic and density profiles. At IGY Camp Michigan, drill core was obtained to nearly 16 meters depth. Annual strata were observed as in the snow pit studies, with ice crusts, layers, and lenses often found to be vertically connected by ice pipes, implying vertical redistribution of meltwater (Zumberge, et al., 1960). Bulk density measurements showed an overall, although discontinuous in detail, increase in density with depth. Studies of four boreholes drilled to 20 meters depth during the traverse program yielded similar results (Crary, et al., 1960). Density-depth studies to much greater depths were carried out at Little America V on the Ross Ice Shelf, at Byrd Station on the mainland ice sheet, and at Ellsworth on the Filchner Ice Shelf (Thiel and Ostenso, 1961; Ragle, et al., 1960). A general logarithmic increase of density with depth was observed, although the curves for the ice shelves exhibit anomolous zones from approximately 40 to 70 meters depth (Figure 6).

#### EFFECT OF GLACIOLOGICAL PARAMETERS ON SEISMIC WAVE PROPAGATION

The density of the surface layers near Minna Bluff is high compared to the rest of the ice shelf, as indicated above. Therefore, somewhat shallower depth penetration

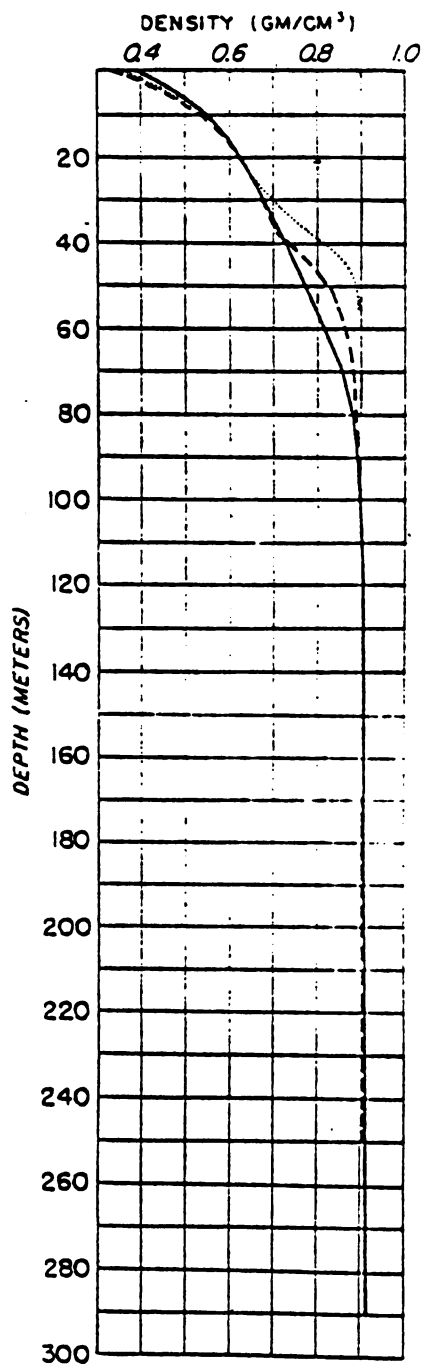


Figure 6

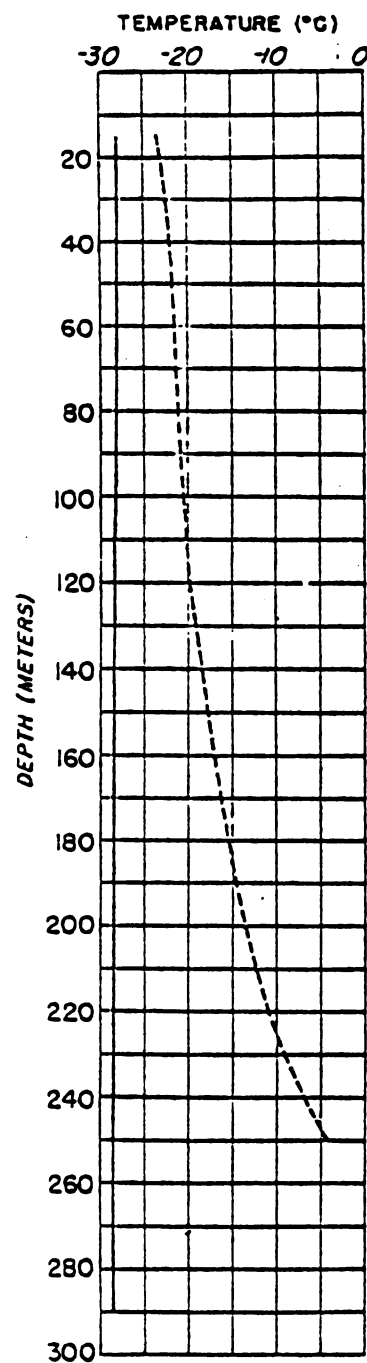


Figure 7

Fig. 6. Density profiles at Byrd Station (solid), Little America V (dashed), and Ellsworth (dotted), (From Thiel and Ostenso, 1961).

Fig. 7. Temperature profile at Byrd (solid) and Little America V (dashed). (From Thiel and Ostenso, 1961)

should be expected for seismic refraction work since maximum density and hence maximum velocity should be achieved at shallower depth relative to the rest of the ice shelf.

The effects of crevasses and fractures on seismic wave propagation in ice have been little investigated. However, from theoretical considerations (Grant and West, 1965; Telford, et al., 1976) certain effects are probable. Open crevasses could completely block seismic wave propagation. Shear waves could be blocked by water-filled crevasses with compressional waves being passed with little if any detectable effect. The lower edges of crevasses entirely closed at depth could produce diffraction effects. To avoid such possible difficulties, the study area was chosen to be outside the crevasse field located east of Minna Bluff (Figure 2), as mentioned above.

Velocity anisotropy could be produced by stratification as discussed by Postma (1955) and in Appendix A. In this regard, Bennett (1968) detected velocity anisotropy in stratified ice from the Ross Ice Shelf, but no axis of symmetry for the variation was identified.

Lower density layers overlain by higher density ice could produce velocity reversals and hidden layers (Telford, et al., 1976). However, if there is a net density increase with depth, as observed, and the low density layers are very thin relative to seismic wavelength, then the effect should be negligible. Since such layers have been observed to be no more than several centimeters thick in the stratigraphic

studies cited above, and the wavelengths involved here are measured in several tens of meters, this is indeed the case. It should also be noted that seismic velocity in ice varies inversely with temperature (Thiel and Ostenso, 1961). As shown in Figure 7 temperature increases with depth in the ice shelf, an effect attributed to the underlying relatively warm ocean. Therefore, velocity reversal at depth should be expected to limit the depths of seismic refraction observations, since density, the other principal factor in velocity, is nearly constant below about 90 meters (Figure 6).

### III. FIELD PROCEDURES

#### FIELD SEASON AND PERSONNEL

The field work for this study was carried out from 26 December 1976 to 3 February 1977 during the Antarctic summer field season. Field personnel consisted of Dr. Hugh Bennett, Dr. Roger Turpening, Jim Adams, John Reed, Barry Prather, and Ron Jennings.

#### DESCRIPTION OF SEISMIC ARRAY, EQUIPMENT, AND PROCEDURES

A radial seismic refraction array consisting of four geophone lines with angular separation of  $45^\circ$  was employed in this study. This pattern was chosen as it facilitates the detection of any directional dependency of seismic velocity. The geophone lines were designated 000, 045, 090, and 135 according to azimuth as measured counterclockwise from line 000, which was oriented east-west. Each line of the array consisted of 24 geophones spaced at 15.24 meter intervals. Three shotpoint locations were laid out in line with and at each end of the geophone lines in order to permit the recording of refraction profiles in both directions along the array. The shotpoints, numbered 1, 2, and 3, were located, respectively, 15.24 meters, 335.28 meters, and 685.80 meters from the ends of the geophone lines. The spacing was chosen to permit a three geophone overlap between seismic records from successive shotpoints on each line.

Seismic records were identified by the array line, the shotpoint, and the letter D (Direct) or R (Reverse),

depending on which end of the array line the shotpoint was located. For example, if the shotpoint was the second on the west end of line 000, the resulting record would be designated 000-2D. The record resulting from the corresponding shotpoint located on the opposite end of the line would be identified as 000-2R. Similarly, proceeding counterclockwise from 000 to 135 the shotpoints have D designations, with those on the opposite ends designated R.

The geophones used, produced by Mark Products, Inc., were characterized by a natural frequency of 4.5 Hz with essentially flat response from 7 Hz to over 100 Hz. Geophone orientation depended upon the seismic wave type whose detection was desired, being vertical for P-wave records, horizontal and normal to the array line for SH-waves, and parallel to the array line for SV-wave records.

The digital recording equipment was furnished by the Environmental Research Institute of Michigan (ERIM). The sampling rate employed for the seismic data was 480 samples per second, resulting in a sampling interval of approximately 2 ms.

Explosives were used to generate the P-wave records. Three pound charges of Nitromon, a product of E.I. DuPont de Nemours, were employed at a shot depth of 3 meters.

For the shear wave records a 4.2 inch mortar, with its base plate seated on the ice, was employed as the seismic energy source. Regulation propellant charges were used to fire plastic containers of a water and ethylene glycol



mixture. For the SH-wave records, the mortar was oriented normal to the geophone line with the barrel at a  $35^\circ$  elevation. An orientation parallel to the geophone line and with the same elevation was used for the SV records. Pairs of seismic records having the first motion of the SH-wave first arrivals breaking in opposite directions (polarity reversal) were obtained for each shotpoint by reversing the direction of the mortar between consecutive shots. Since everything else was the same between shots, the arrival times for seismic events at the same geophone locations should likewise be identical. Therefore, positive identification of shear waves on the plotted seismic sections and increased accuracy of arrival time determination were made possible. The procedures for SV-waves were similar except for mortar and geophone orientation as noted above.

#### DISTANCE AND TIME MEASUREMENT

Distances were measured in the field by steel tape. Wooden dowels were used to mark measured locations.

Arrival times were measured directly on seismic sections prepared by ERIM from digital field tapes. For a detailed description of the techniques followed in event recognition and time measurement, see Appendix C.

Error estimates have been made for distance, time, and velocity measurement. The error in distance measurement was estimated in the field by triangulation and remeasurement to be  $\pm 0.01\%$  (H. Bennett, personal communication).

Time-distance (T-X) curves prepared from arrival time data (Appendix D) exhibit linear and non-linear segments. Error was estimated for the linear segments by determining the standard deviation of the measured time values from the best straight line fitted to the data by least squares. For the non-linear segments, estimation of error in time measurement was by determination of the standard deviation of the measured times from the visually best fitted curve. Estimated time error for both P and SH-waves is  $\pm 0.8$  ms for the linear segments and  $\pm 1.0$  ms for the non-linear segments. The resulting velocity error for the linear segments is estimated at  $\pm 0.3\%$  and  $\pm 0.2\%$  for SH and P-wave velocities, respectively (Chapter 5). Error in velocities for the non-linear segments is discussed in Chapter 5.

Since the error in distance measurement is not more than 5% of the error in time measurement as estimated above, this error may be considered negligible for the purposes of this study. Distances will therefore be assumed to be accurate. All error is thus considered to arise in time measurement.

#### IV. DATA REDUCTION: TIME-DISTANCE CURVES

##### INTRODUCTION

Compressional and SH-wave records were chosen for this study on the basis of preliminary evaluation of the seismic sections prepared by ERIM. Time-distance (T-X) curves, discussed below, were prepared for both P- and SH-waves. The T-X curves were analyzed to produce velocity-depth curves (Chapter 5).

##### DISCUSSION OF TIME-DISTANCE CURVES

The T-X curves (Figures 8-12), initially non-linear, become linear with distance from the shotpoint. That point on the curve joining the linear and non-linear segments will herein be termed the breakpoint. The breakpoint for each curve was determined analytically. The data for each curve was fitted by least squares to a line of the form:

$$T = mx + b$$

where: T = arrival time in seconds

m = slope

x = shotpoint-receiver distance

b = T axis intercept

Beginning with the T-X data point at X = 609.60m, points were successively fitted in the -X direction. The linear correlation coefficient (r) was computed after each successive data point had been fitted. The correlation coefficient defined (Crow, et al., 1960) by:

$$r = \frac{n\sum XT - (\sum X)(\sum T)}{\left[ n\sum X^2 - (\sum X)^2 \right]^{\frac{1}{2}} \left[ n\sum T^2 - (\sum T)^2 \right]^{\frac{1}{2}}}$$

where, in this case,  $X$  = shotpoint to receiver distance,  $T$  = arrival time, and  $n$  = number of data points, indicates how well the data points fit the least squares regression line. Hence, if successive data points are increasingly non-linear, then  $r$  should decrease in magnitude in a continuous manner. The point at which such a decrease was observed to begin was selected as the breakpoint. Two sets of SH-wave data were thus indicated, one with the breakpoint at  $X = 140.97\text{m} \pm 14.59\text{m}$  (Set A)(Figures 8 and 10-A,B,E,F), and one with the breakpoint at  $X = 297.18\text{m} \pm 26.40\text{m}$  (Set B) (Figures 9 and 10-C,D,G,H). Set A, plotted in Figure 8, corresponds to the 000 and 090 array directions, with Set B, plotted in Figure 9, corresponding to the 045 and 135 directions. One data set was indicated for the P-waves (Figures 11-A and 11-B with breakpoint at  $106.68\text{m} \pm 8.15\text{m}$ ).

The reciprocal of the slope of a time-distance curve at a given distance from the shotpoint is the maximum velocity penetrated by the raypath from the shotpoint to a receiver at that location (Telford, et al., 1976). Since, in this case, the  $T$ - $X$  curve slope is constant beyond the breakpoint, it is assumed that maximum velocity has been reached for the entire curve at this point. Maximum velocities were determined for each curve by computing the reciprocal of the slope of the line fitted by least squares from the breakpoint to the end of the curve (Tables I and II).

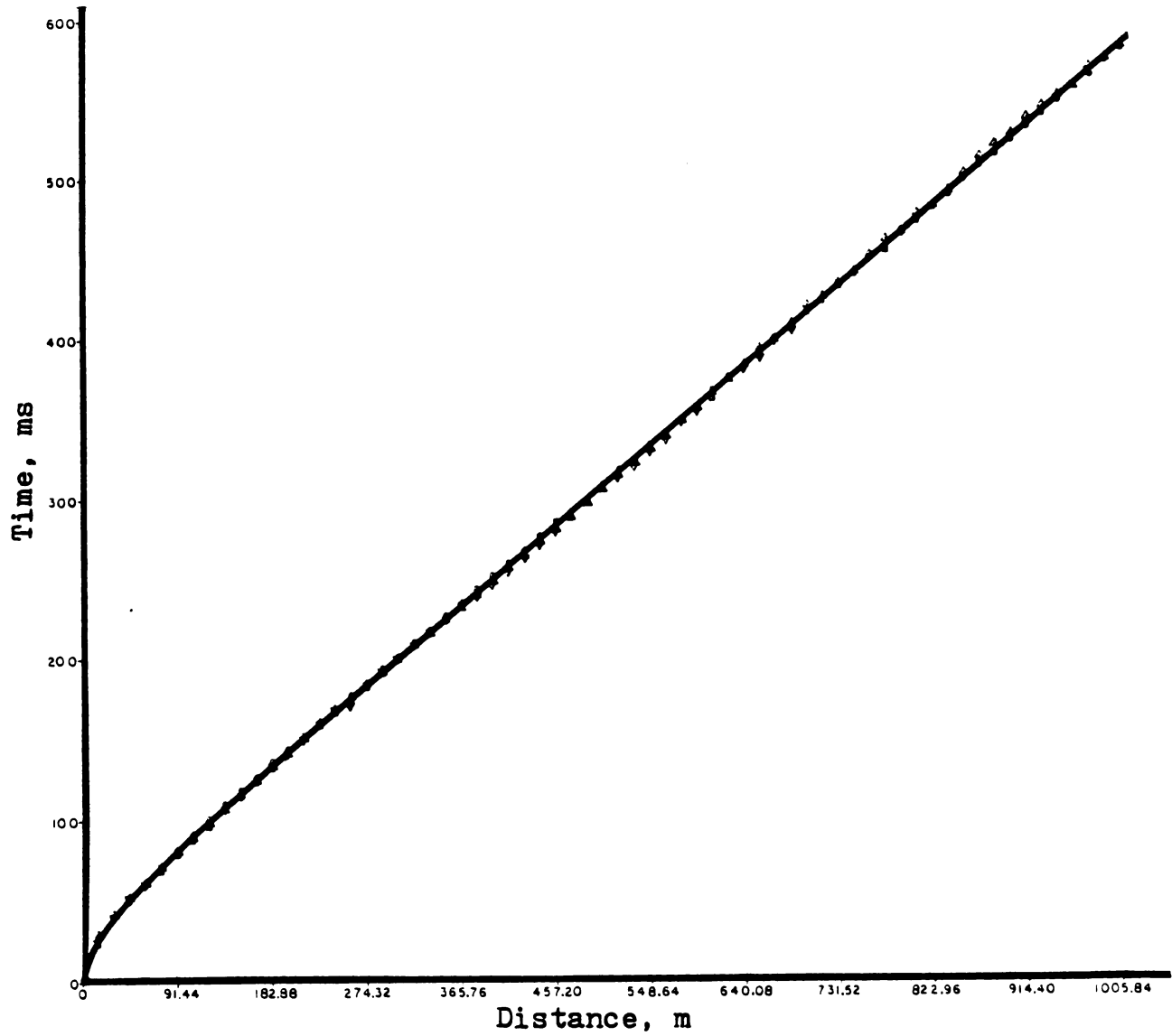


Figure 8. T-X curve, SH waves Set A: 000-090 directions.

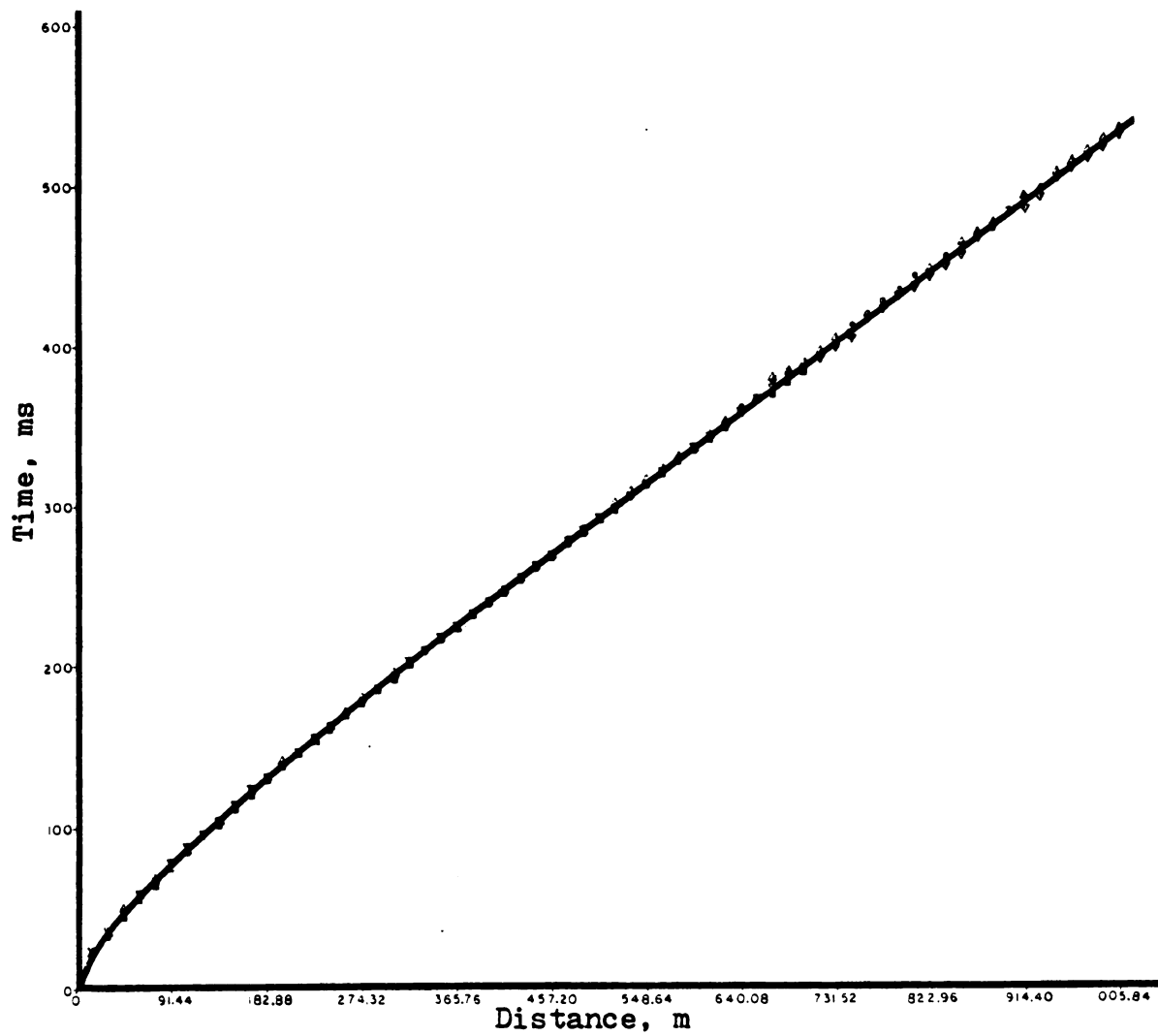


Figure 9. T-X curve, SH waves Set B: 045-135 directions.

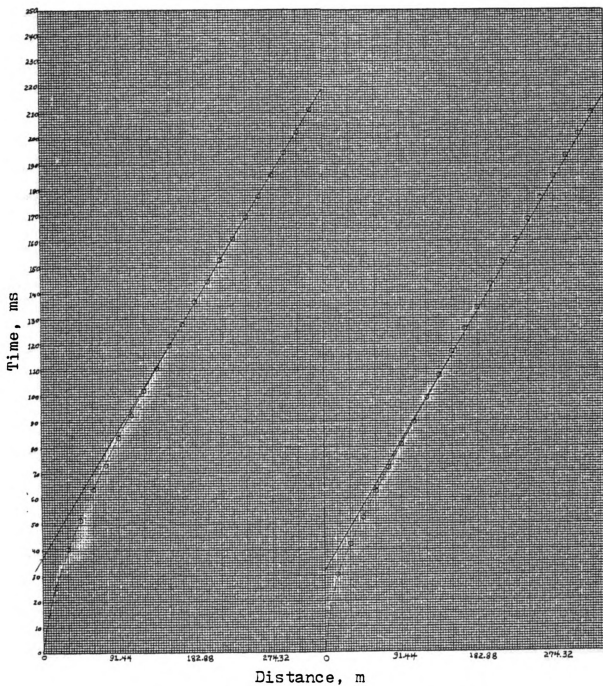


Figure 10-A

Figure 10-B

Fig. 10-A. T-X curve, non-linear part, SH-000-D

Fig. 10-B. T-X curve, non-linear part, SH-000-R

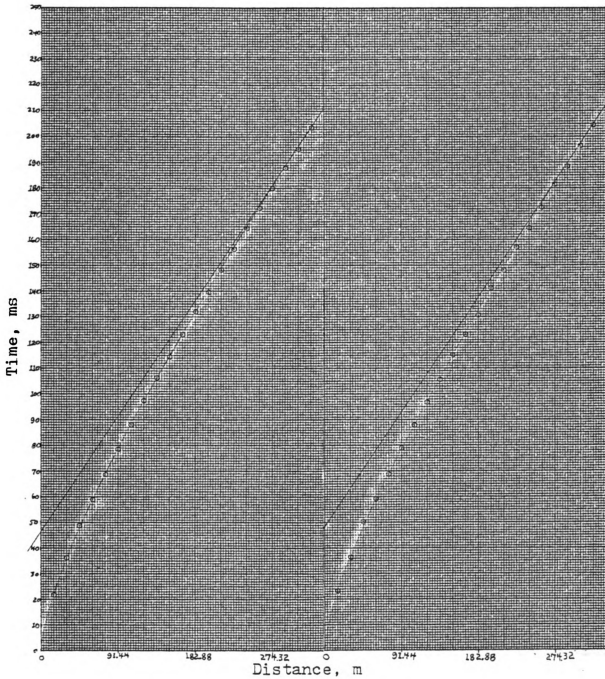


Figure 10-C

Figure 10-D

Fig. 10-C. T-X curve, non-linear part, SH-045-D

Fig. 10-D. T-X curve, non-linear part, SH-045-R



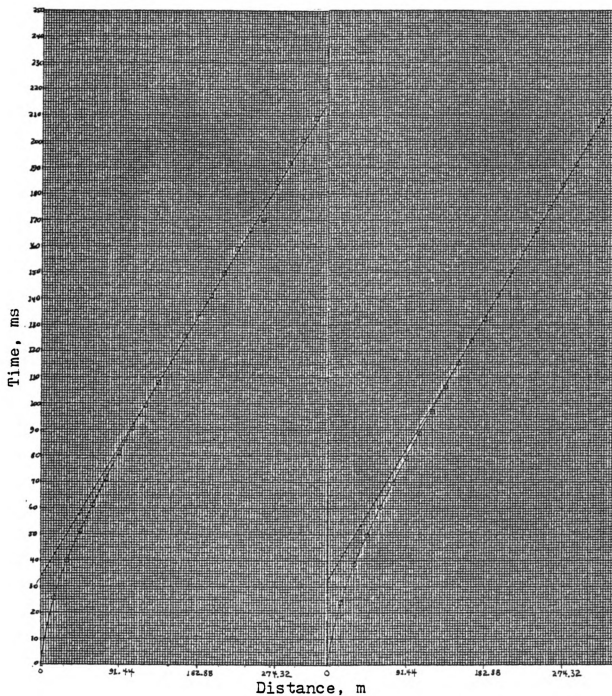


Figure 10-E

Figure 10-F

Fig. 10-E. T-X curve, non-linear part, SH-090-D

Fig. 10-F. T-X curve, non-linear part, SH-090-R

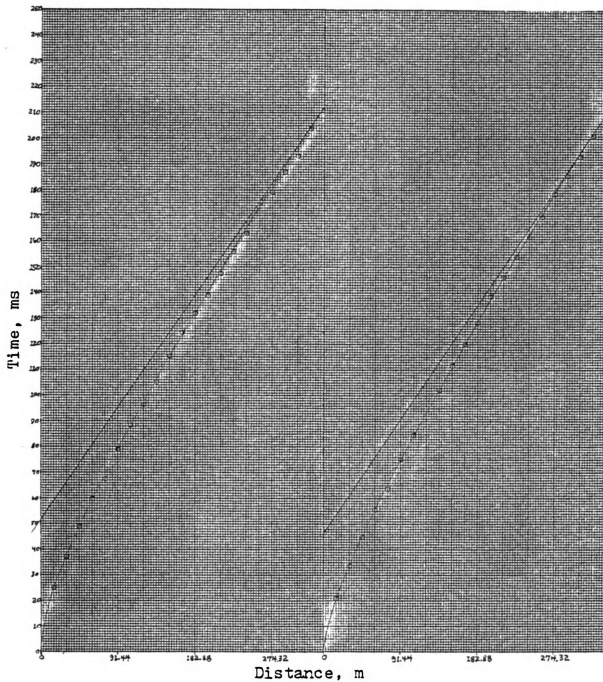


Figure 10-G

Figure 10-H

Fig. 10-G. T-X curve, non-linear part, SH-135-D

Fig. 10-H. T-X curve, non-linear part, SH-135-R

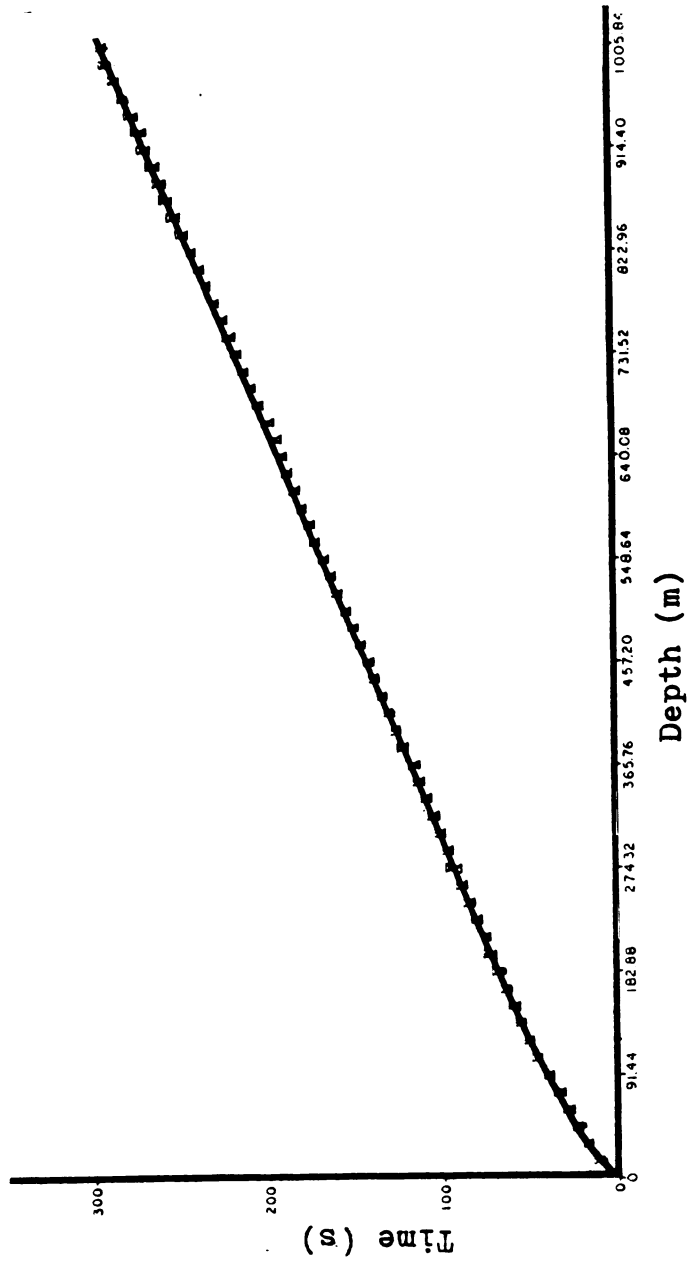


Figure 11-A. P-Wave T-X curve, 000 and 090 directions.

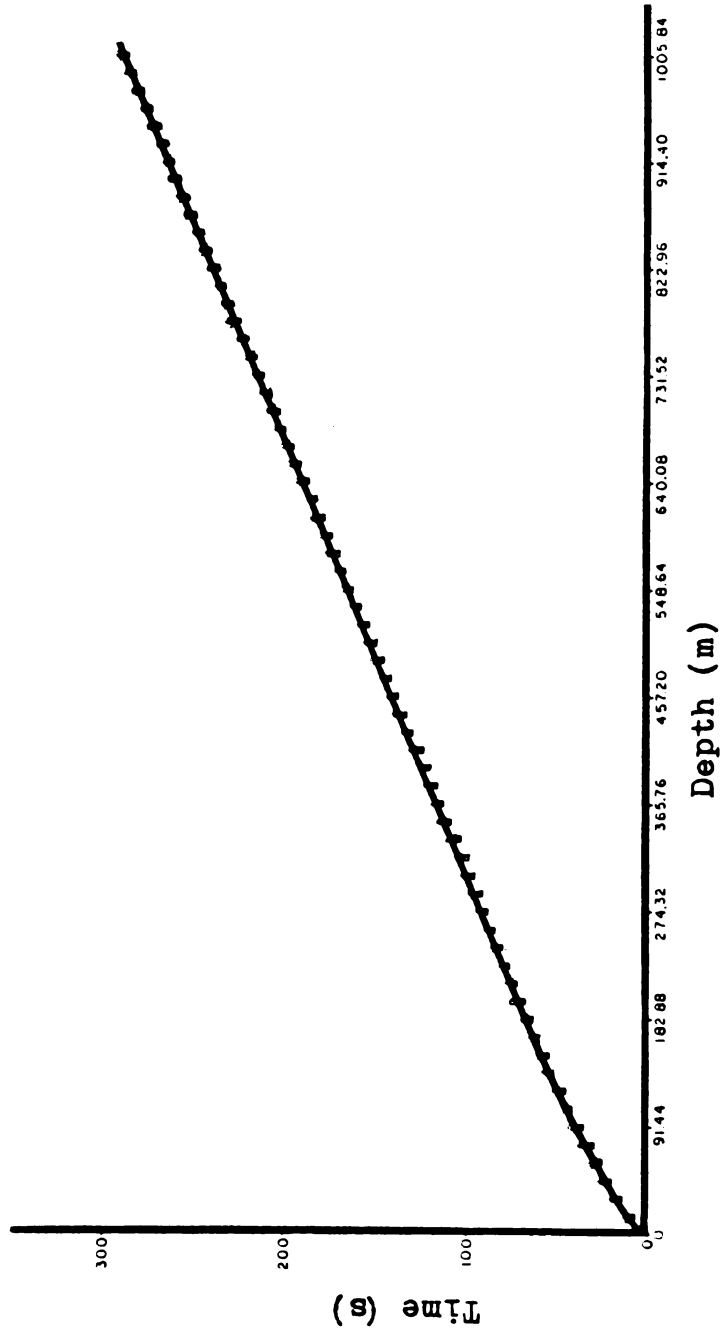


Figure 11-B. P-Wave T-X curve, 045 and 135 directions.

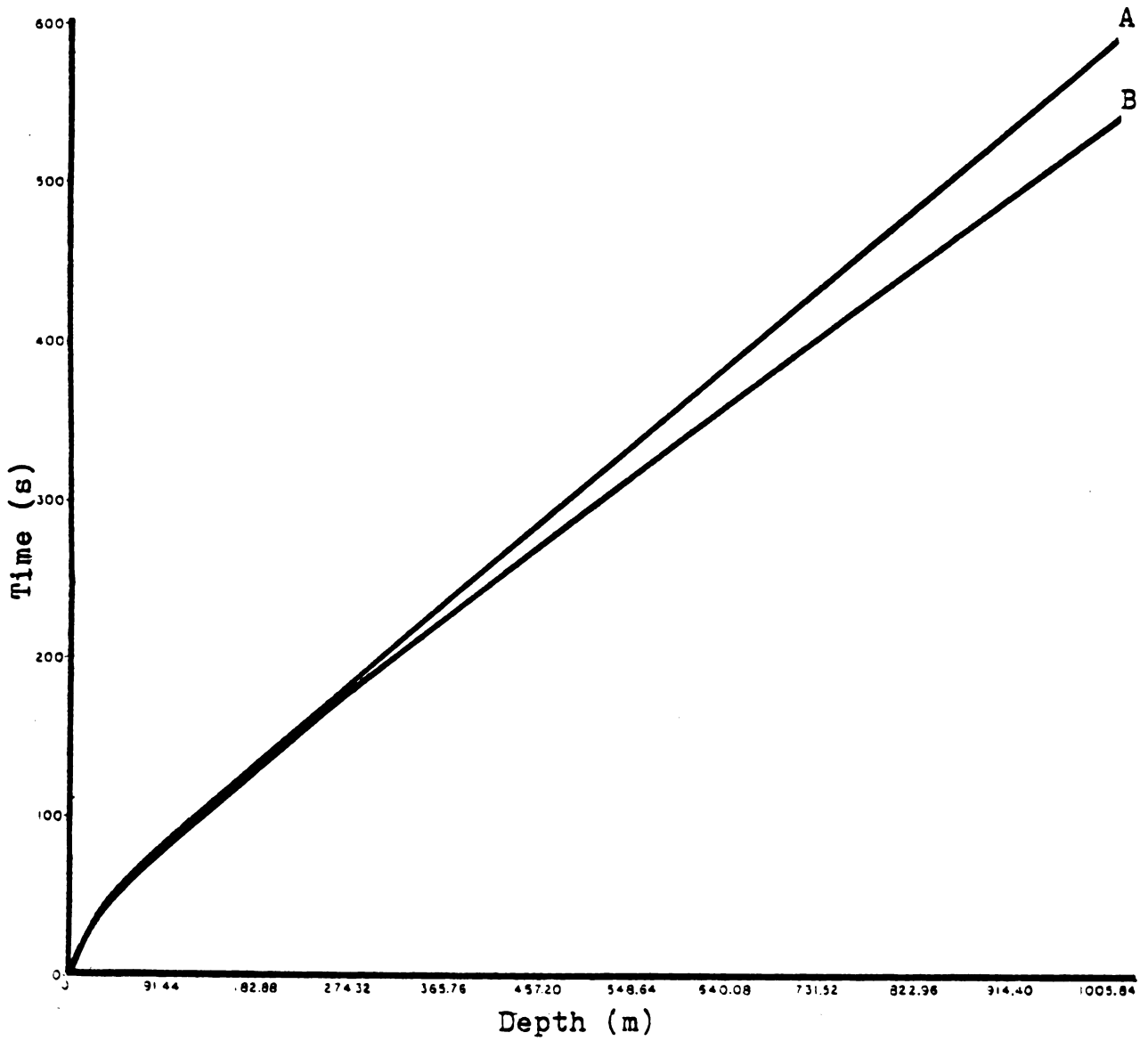


Figure 12. Best Fit Curves, Shear Wave Set A and B.

Maximum SH-wave velocity thus computed varied in a centro-symmetric fashion about the array. Two data sets were apparent, corresponding to Sets A and B above, with Set B velocities greater than those of Set A. As seen from Table I, the greatest difference in maximum SH-wave velocity for the array is  $276.7\text{ms}^{-1}$ , or about 15.3% occurring between the 000-R and 135-D directions. Mean velocity for Set A is  $1829.5\text{ms}^{-1} \pm 14.86\text{ms}^{-1}$ , while that of Set B is  $2056.4\text{ms}^{-1} \pm 24.2\text{ms}^{-1}$ , or about 12.4% greater. Composite T-X curves for the two sets, prepared by fitting all data in each set by least squares beyond the breakpoint and visually fitting the non-linear segment, are plotted in Figure 12, with maximum velocities given in Table I.

Compressional wave maximum velocities (Table II) varied with direction, but did not exhibit centro-symmetry. However, the P-wave data exhibits shingling in the linear part of all curves except 135R. Successive linear segments (shingles) having the same slope are shifted down 2 ms with respect to the preceding linear segment. This results in the overall slope of the line decreasing, and hence the velocity increasing, with each additional shingle. The number of shingles per curve varies from zero to 4. Thus, it would be expected that the maximum velocities computed from the raw data depend significantly on the shingling (Table II A). By applying successive 2, 4, 6, and 8 ms corrections as needed, the shingles may be shifted back into one line. Maximum velocities thus computed were found to be nearly

SH-WAVES: REGRESSION LINES AND MAXIMUM VELOCITIES

TABLE I

<u>Line</u>	<u>m</u>	<u>b</u>	<u><math>\bar{v}</math></u>	<u>r</u>	<u>Break-point</u>
000D	0.0001656848	0.0370882034	1839.6	0.999991	137.16
000R	0.000168308	0.0319356488	1810.9	0.999927	152.40
090D	0.0001653559	0.0339135756	1843.3	0.999869	121.92
090R	0.0001670867	0.0328314292	1824.2	0.999974	152.40
045D	0.0001501921	0.0465203385	2029.4	0.999905	274.32
045R	0.000148703	0.0486235916	2049.7	0.999908	274.32
135D	0.0001459978	0.0517536593	2087.7	0.999885	320.04
135R	0.0001480648	0.0466262903	2058.6	0.999953	320.04

P-WAVES: REGRESSION LINES AND MAXIMUM VELOCITIES

TABLE II-A (SHINGLING PRESENT)

<u>Line</u>	<u>m</u>	<u>b</u>	<u><math>\bar{v}</math></u>	<u>r</u>	<u>Break-point</u>
000D	0.0214274878	0.0000802895	3796.3	0.999902	121.92
000R	0.0218468894	0.0000793171	3842.8	0.999908	91.44
090D	0.0204982104	0.0000796083	3828.7	0.999940	106.68
090R	0.0168963888	0.0000811375	3756.6	0.999949	106.68
045D	0.018222967	0.0000816989	3730.8	0.999904	106.68
045R	0.0000836222	0.0157131531	3645.0	0.999940	106.68
135D	0.019456133	0.0000813077	3748.7	0.999894	106.68
135R	(no shingling observed)				

TABLE II-B (SHINGLING NOT PRESENT)

<u>Line</u>	<u>m</u>	<u>b</u>	<u><math>\bar{v}</math></u>	<u>r</u>	<u>Break-point</u>
000D	0.0000829497	0.0187043464	3674.5	0.999991	121.92
000R	0.000082862	0.0168198662	3678.4	0.999980	91.44
090D	0.0000823795	0.0173331777	3699.9	0.999995	106.68
090R	0.0000829898	0.0145586475	3672.7	0.999998	106.68
045D	0.0000827115	0.0169785599	3685.1	0.999997	106.68
045R	0.0000833153	0.0164307294	3658.4	0.999969	106.68
135D	0.0000835575	0.0158197548	3647.8	0.999919	106.68
135R	0.0000833862	0.0184724438	3655.3	0.999874	106.68

the same, with a maximum difference of  $52.1 \text{ ms}^{-1}$  ( $\approx 1.4\%$ ), and a mean velocity for the entire array of  $3671.3 \pm 18.1 \text{ ms}^{-1}$  (Table II B). The variation in velocity with direction appears random.

As to the causes of the shingling phenomenon, a full discussion and analysis is beyond the scope of this report, but certain conjectures may be made. Spencer (1965) showed that such an effect in a P-wave refraction profile may result from multiple reflections within a high-speed layer. According to this theory, where such a layer is present and is several wavelengths in thickness, the refracted arrival may consist of a series of events separated by a constant time interval. Each such shingle is produced by superposition of P-S converted waves multiply reflected the same number of times within the layer while in the shear mode. Such a layer within the ice shelf could be visualized as forming at the surface during a time of warmer climate in the past. Fairly extensive melting and refreezing of surface layers into a thick, dense ice layer, later buried by annual snow accumulation, would be required. However, as no other evidence for such a layer has been found, and as the thickness of the layer would at least have to approach that of the wavelengths involved, here about 80 m, such a model should be considered very tentative and quite questionable.



## V. ANALYSIS AND INTERPRETATION

### INTRODUCTION

SH and P-wave velocity-depth (V-Z) profiles are presented in this chapter for each array direction. The profiles are discussed and a model proposed to explain the results in Chapter 6. The Weichert-Herglotz-Batemann (WHB) integral method (Appendix B) was used to compute the V-Z profiles. This method requires a knowledge of the increase of velocity with distance up to the maximum velocity for each curve. Therefore, the velocities were determined at evenly-spaced consecutive points along the non-linear portion of each T-X curve. The method of velocity determination is discussed in the following section, and error is estimated for both velocity and depth.

### VELOCITY DETERMINATION AND ERROR ANALYSIS

The velocities for the non-linear portions of each T-X curve were determined graphically. A T-X plot was constructed for each non-linear segment with the data points plotted to a precision of  $\pm 0.1$  ms. A smooth curve was then visually fitted to each plot (Figures 10-A to 10-H, for example). The velocity was determined along the curves every 15.24 m, corresponding to geophone spacing, as follows. A straight-edge was visually aligned tangent to the curve at each such point. The tangent line was fitted first without optical aids, then the fit at and near the point was examined under 5X magnification, to verify precise placement of the

straight-edge, and adjusted if necessary. The velocity at each point was computed by the formula:

$$V_{x_i} = \frac{x_i}{t_{x_i} - t_0}$$

where:  $x_i$  = distance from the origin

$t_{x_i}$  = time intercepted by the tangent line at  $x_i$

$t_0$  = the T-axis intercept time

The times,  $t_{x_i}$  and  $t_0$  were read directly from the graph to  $\pm 0.1$  ms precision.

Error in the velocities thus determined, as well as error in maximum velocity, has been estimated and is discussed in the following paragraphs. The resulting error in depths computed by the WHB method will also be evaluated.

Error in time measurement was estimated to be  $\pm 0.8$  ms for the linear portions of the T-X curves (Chapter 3). The resulting error in maximum velocity may be estimated as follows, where  $v$ ,  $x$ , and  $t$  are velocity, distance, and time respectively.

$$v = \frac{x}{t}$$

therefore:

$$\frac{dv}{dt} = \frac{dt}{tdt} - \frac{x}{t^2}$$

$$dv = \frac{dx}{t} - \frac{xdx}{t^2}$$

$$\frac{dv}{v} = \frac{dx}{x} \cdot \frac{t}{x} - \frac{xdx}{t^2} \cdot \frac{t}{x}$$

$$\frac{dv}{v} = \frac{dx}{x} - \frac{dt}{t}$$

For  $\Delta v, \Delta x, \Delta t$  very small, this may be approximated by:

$$\frac{\Delta v}{v} = \frac{\Delta x}{x} - \frac{\Delta t}{t}$$

Since distance is assumed accurate with respect to timing errors (Chapter 3), the first term on the right can be neglected, and

$$\frac{\Delta v}{v} = - \frac{\Delta t}{t}$$

Therefore, where  $\Delta v$  is velocity error, and  $\Delta t = \pm \Delta t_e$  = time error, the % error in velocity is given by:

$$E_v = \frac{\Delta v}{v} \cdot 100 = \pm \frac{\Delta t_e}{t} \cdot 100$$

$$\text{Average velocity } \bar{v} = \frac{x}{t}, \therefore \frac{1}{t} = \frac{\bar{v}}{x}$$

$$\text{thus, } E_v = \pm \frac{\bar{v} \Delta t_e}{x} \cdot 100 \quad (1)$$

where  $\bar{v}$  is the velocity determined by least squares for the linear segment of a T-X curve and  $x$  is the length of the linear segment, (1) gives the percent velocity error. The application of this formula to the T-X curves yielded an error in maximum velocity of  $\pm 0.3\%$  for the P-waves, and  $\pm 0.2\%$  for the SH-waves.

The velocities determined for the non-linear portions of the T-X curves were used to compute the WHB profiles, as stated above. For velocities less than maximum velocity ( $V_m$ ), error was estimated by determining the standard deviation of velocity at selected depths on the V-Z profiles. Percent velocity error was estimated as  $\frac{\sigma_z}{\bar{v}_z}$ , where  $\bar{v}_z$  = mean velocity at depth  $z$ , and  $\sigma_z$  = standard deviation of

velocity at depth  $z$ . The associated depth error was similarly estimated by standard deviation of depth at selected velocities on the V-Z profile. Percent error in depth was estimated as  $\frac{\sigma_v}{Z_v}$ , where  $Z_v$  = mean depth at which velocity  $v$  occurs, and  $\sigma_v$  = standard deviation of depth at which that velocity is reached. This is thought to represent a reasonable estimate of total error, since the computed V-Z profile incorporates all errors affecting velocities from  $V_0$  to  $V_m$ .

The results of the error analysis appear in Table III and Figures 13A and 13B. SH-wave velocity error ranges from  $\pm 8.8\%$  at the surface to  $\pm 0.2\%$ , as noted above, at maximum depth. Depth error for SH-waves exhibits a range of  $\pm 25.0\%$  for a velocity of  $500 \text{ ms}^{-1}$  to  $\pm 7.5\%$  and  $\pm 5.3\%$  at maximum velocity for Set A and Set B, respectively. P-wave velocity error ranges from  $\pm 25.4\%$  at the surface, to  $\pm 0.3\%$ , as noted above, at maximum depth. Error in P-wave depth was estimated at  $\pm 40\%$  at  $1000 \text{ ms}^{-1}$ , with an error of  $\pm 6.8\%$  at maximum velocity. For depths greater than 20 m, P and SH-wave velocity error is less than  $4\%$ , while depth error is not more than  $7\%$ . It is readily concluded from Table III and Figures 13A and 13B that velocity error decreases with depth, while accuracy of depth determination increases with velocity. The large magnitude of the estimated error in both velocity and depth for P and SH-waves above 20 m is largely attributable to the inhomogeneous nature of the near-surface layers of the ice shelf, such as described in snow-pit studies by Crary. et. al., (1963).

ERROR ANALYSIS

TABLE III

<u>SH-WAVES: VELOCITY ERROR *</u>										
<u>Z(m)</u>	<u>000D</u>	<u>000R</u>	<u>045D</u>	<u>045R</u>	<u>090D</u>	<u>090R</u>	<u>135D</u>	<u>135R</u>	<u><math>V \pm \sigma_z</math></u>	<u><math>\frac{\sigma_z}{V}</math></u>
0	305.7	287.5	305.4	338.7	345.2	350.3	326.0	363.7	$327.8 \pm 26.3$	8.9%
10	995	1100	1075	1115	1035	1040	1150	1175	$1085.6 \pm 61.2$	5.6%
20	1410	1583	1450	1495	1490	1490	1515	1525	$1494.8 \pm 51.2$	3.4%
30	1665	1775	1663	1690	1720	1700	1695	1715	$1702.9 \pm 35.7$	2.1%
40			1785	1800			1800	1820	$1801.3 \pm 14.4$	0.8%
50			1875	1885			1897	1895	$1880.0 \pm 10.1$	0.5%
60			1955	1962			1975	1963	$1964.8 \pm 8.3$	0.4%
<u>SH-WAVES: DEPTH ERROR**</u>										
<u>V(ms<sup>-1</sup>)</u>	<u>000D</u>	<u>000R</u>	<u>045D</u>	<u>045R</u>	<u>090D</u>	<u>090R</u>	<u>135D</u>	<u>135R</u>	<u><math>Z_v \pm \sigma_v</math></u>	<u><math>\frac{\sigma_v}{Z_v}</math></u>
500	2.6	2.4	2.2	1.5	2.2	2.0	1.6	1.2	$2.0 \pm 0.5$	25 %
1000	10.1	8.5	8.7	7.8	9.4	9.3	7.5	7.0	$8.5 \pm 1.0$	11.9%
1500	23.3	17.7	21.4	20.2	20.3	20.4	18.3	19.0	$20.0 \pm 1.8$	9 %
$V_m(A)$	33.7	39.8			36.3	38.9			$37.2 \pm 2.8$	7.5%
$V_m(B)$			66.7	67.2			74.1	72.5	$70.1 \pm 3.7$	5.3%
<u>P-WAVES: VELOCITY ERROR *</u>										
<u>Z(m)</u>	<u>000D</u>	<u>000R</u>	<u>045D</u>	<u>045R</u>	<u>090D</u>	<u>090R</u>	<u>135D</u>	<u>135R</u>	<u><math>V_z \pm \sigma_z</math></u>	<u><math>\frac{\sigma_z}{V_z}</math></u>
0	641.7	612.0	680.4	677.3	762.0	1172.3	655.5	937.8	$729.9 \pm 184.3$	25.4%
10	2090	2060	2150	2225	2115	2495	2035	2185	$2169.4 \pm 145.9$	6.7%
20	2780	2850	2855	2920	2845	3020	2895	2795	$2870 \pm 76.2$	2.7%
30	3280	3470	3405	3400	3373	3450	3475	3295	$3393.5 \pm 74.5$	2.2%
<u>P-WAVES: DEPTH ERROR**</u>										
<u>V(ms<sup>-1</sup>)</u>	<u>000D</u>	<u>000R</u>	<u>045D</u>	<u>045R</u>	<u>090D</u>	<u>090R</u>	<u>135D</u>	<u>135R</u>	<u><math>Z_v \pm \sigma_v</math></u>	<u><math>\frac{\sigma_v}{Z_v}</math></u>
1000	1.3	2.2	1.7	1.6	1.4		1.3	0.3	$1.5 \pm 0.6$	40 %
2000	9.1	9.4	8.5	8.0	8.9	4.9	9.7	7.8	$8.3 \pm 1.5$	18.1%
3000	24.2	22.3	22.5	21.4	22.7	19.6	21.4	24.0	$22.3 \pm 1.5$	6.7%
$V_m$	40.0	32.4	35.6	34.7	36.0	32.9	33.8	36.2	$35.2 \pm 2.4$	6.8%

\* Columns 000D through 135R are velocities in  $\text{ms}^{-1}$  at depth Z.

\*\* Columns 000D through 135R are depths in m at velocity V.

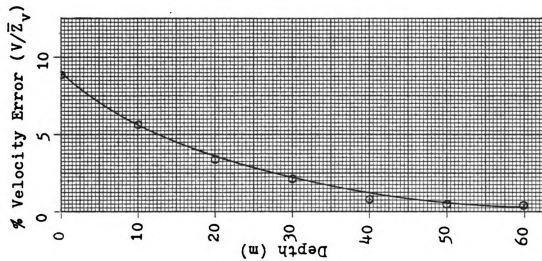


Figure 13-A. Depth vs Error, SH-Waves.

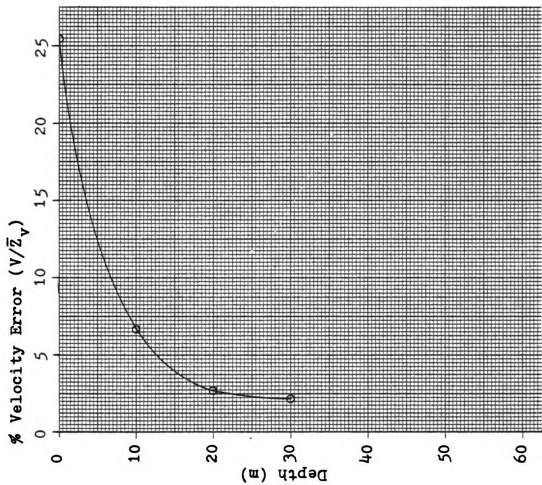


Figure 13-B. Depth vs Error, P-Waves.

VELOCITY-DEPTH PROFILES

The WHB integral, derived in Appendix B, was used to compute P and SH-wave velocity-depth profiles for all array directions. The integral is defined as:

$$Z_n = \frac{1}{\pi} \int_0^{x_n} \cosh^{-1}\left(\frac{V_{x_n}}{V_{x_i}}\right) dx ,$$

where:  $V_{x_n} = \left. \frac{dx}{dt} \right|_{x=x_n}$  = maximum velocity sampled by the raypath from shotpoint to receiver at range  $x_n$ .

$V_{x_i} = \left. \frac{dx}{dt} \right|_{x=x_i}$  = velocity at  $x_i$ ,  $0 \leq i \leq n$ .

$Z_n$  = depth at which  $V_{x_n}$  is penetrated.

The integral is obviously of such a form that it may be directly computed numerically (Grant and West, 1965). Numerical computation may be implemented by:

$$Z_n = \frac{\Delta x}{\pi} \sum_{i=0}^n \cosh^{-1}\left(\frac{V_{x_n}}{V_{x_i}}\right)$$

$$Z_n = \frac{\Delta x}{\pi} \sum_{i=0}^n \ln \left[ \frac{V_{x_n}}{V_{x_i}} + \left\{ \left( \frac{V_{x_n}}{V_{x_i}} \right)^2 - 1 \right\}^{\frac{1}{2}} \right] \quad (2)$$

where:  $\Delta x$  = spacing between V-x data points

$n$  = number of data points

$Z_n$ ,  $V_{x_n}$ , and  $V_{x_i}$  are as above.

In the calculation,  $V_{x_n}$  is fixed for any given raypath, and  $V_{x_i}$  ranges from  $V_0$  to  $V_{x_n}$ . Thus, for any given  $V_{x_n}$ , all previous  $V_{x_i}$  determined from the T-X curve are used in the integration. For this study, a program for the automatic computation of the integral using equation (2) was written

for a Texas Instruments Ti-58 programmable calculator with PC-100A printer, with which all profiles were calculated. The tabulated results appear in Appendix E.

The velocity-depth profiles are presented in Figures 14-A to 14-H for P-waves, and in Figures 15-A to 15-H for SH-waves. It is readily observed that the SH-wave curves fall into two groups, corresponding with T-X data Sets A and B of the preceeding chapter. For Set A (Figures 15-A, B, E, F & 16) maximum velocity is reached at a mean depth of  $37.2 \text{ m} \pm 2.8 \text{ m}$ , whereas for Set B (Figures 15-C, D, G, H, & 17),  $V_m$  occurs at a mean depth of  $70.1 \text{ m} \pm 3.7 \text{ m}$ . Depth to P-wave maximum velocity is nearly the same for all array directions, with a mean of  $35.2 \text{ m} \pm 2.4 \text{ m}$ . The implications of these results are discussed in depth in the next chapter.



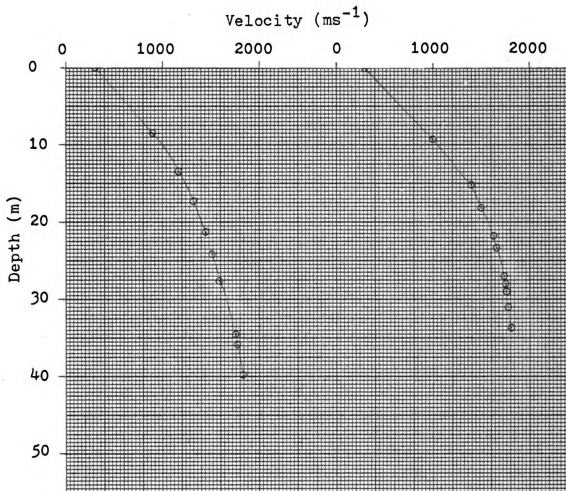


Figure 14-A

Figure 14-B

Figure 14-A. Velocity-Depth Profile: Line SH-000-D.

Figure 14-B. Velocity-Depth Profile: Line SH-000-R.

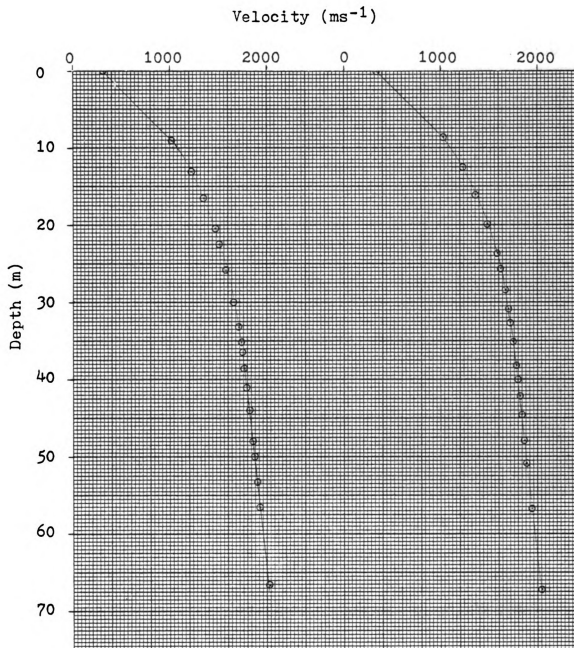


Figure 14-C

Figure 14-D

Figure 14-C. Velocity-Depth Profile: Line SH-045-D.

Figure 14-D. Velocity-Depth Profile: Line SH-045-R.

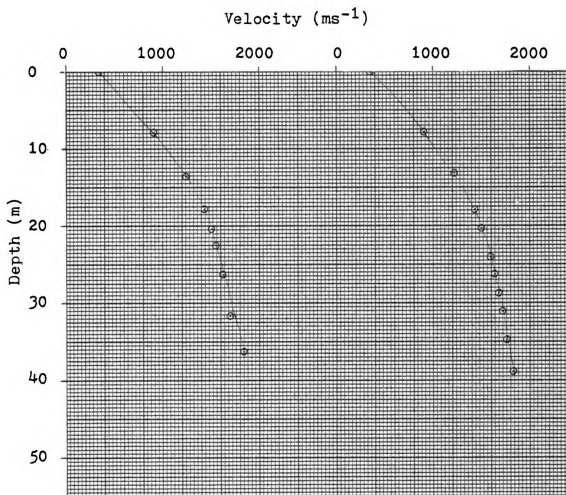


Figure 14-E

Figure 14-F

Figure 14-E. Velocity-Depth Profile: Line SH-090-D.

Figure 14-F. Velocity-Depth Profile: Line SH-090-R.

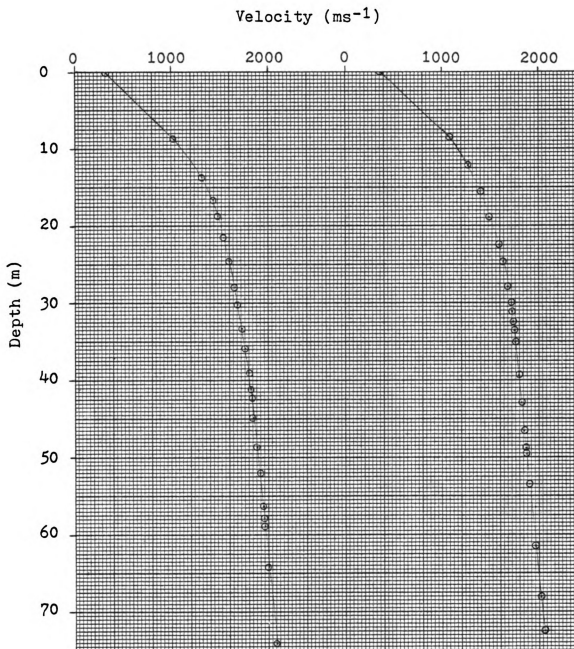


Figure 14-G

Figure 14-H

Figure 14-G. Velocity-Depth Profile: Line SH-135-D.

Figure 14-H. Velocity-Depth Profile: Line SH-135-R.

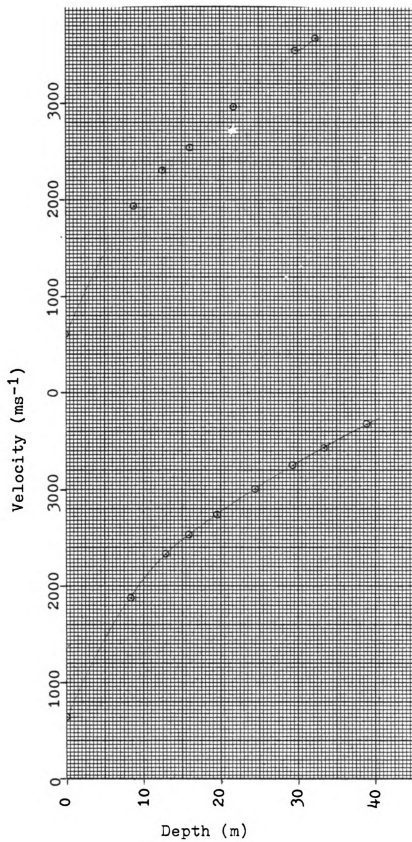


Figure 15-A

Figure 15-B

Fig. 15-A. Velocity-Depth Profile: Line P-000-D.

Fig. 15-B. Velocity-Depth Profile: Line P-000-R.

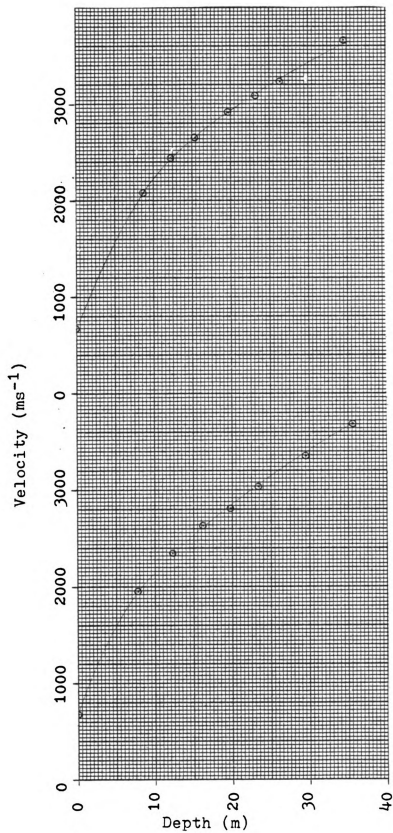


Figure 15-C

Figure 15-D

Fig. 15-C. Velocity-Depth Profile: Line P-045-D

Fig. 15-D. Velocity-Depth Profile: Line P-045-R.

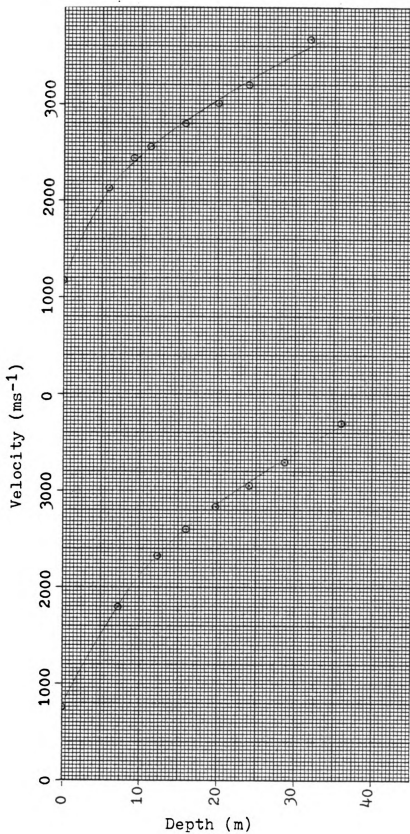


Figure 15-E

Figure 15-F

Fig. 15-E. Velocity-Depth Profile: Line P-090-D.

Fig. 15-F. Velocity-Depth Profile: Line P-090-R.

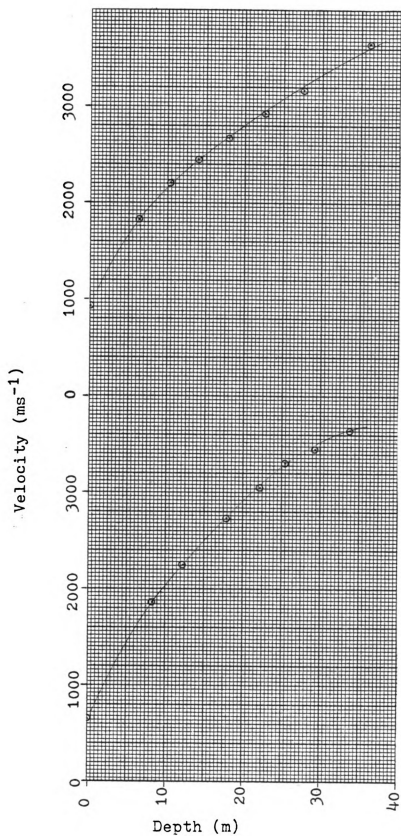


Figure 15-G

Figure 15-H

Fig. 15-G. Velocity-Depth Profile: Line P-135-D.

Fig. 15-H. Velocity-Depth Profile: Line P-135-R.



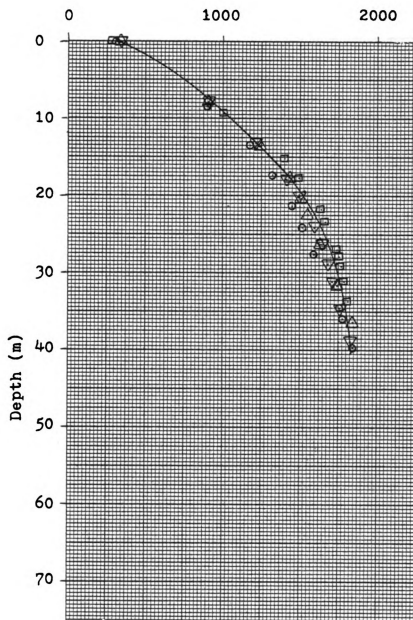
Velocity ( $\text{ms}^{-1}$ )

Figure 16. Velocity-Depth Profile: SH-Waves Set A.

○ SH-000-D      □ SH-000-R  
△ SH-090-D      ▽ SH-090-R

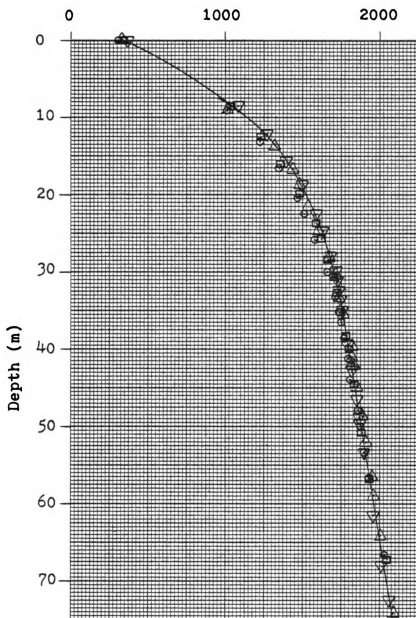
Velocity ( $\text{ms}^{-1}$ )

Figure 17. Velocity-Depth Profile: SH-Waves Set B.

○ SH-045-D    □ SH-045-R  
△ SH-135-D    ▽ SH-135-R

## INTERPRETATION OF VELOCITY-DEPTH PROFILES: DEVELOPMENT OF MODEL

### A. VELOCITY INCREASE TO 37 M DEPTH: DENSIFICATION

Compressional and SH-wave velocities are, on the average, 60% of their maximum value at 10 m depth, and 80% of maximum velocity is attained at 20 m depth (Table III). Maximum velocity for both wave types is reached at about 37 m, considering only the Set A shear wave maximum velocity. Thus, velocity increases very rapidly with depth, with the rate of increase falling quickly below about 15 m depth, as is readily seen in Figures 14 through 17.

Studies on the Ross Ice Shelf at Little America V and along the IGY traverses, at Ellsworth Station on the Filchner Ice Shelf, at Byrd Station on the Marie Byrd Land Ice Sheet, in Greenland, and elsewhere have repeatedly demonstrated the rapid initial increase of density with depth (Robin, 1958; Crow, 1960; Ragle, et. al., 1960; Thiel and Ostenso, 1961; Crary, et. al., 1962; Kohnen and Bentley, 1973). Densification of snow in general initially proceeds rapidly with depth by mechanical repacking of grains as load increases, until a density of  $0.55 \text{ gm cm}^{-3}$  is reached, which represents the limit below which further porosity reduction is not possible by repacking alone (Paterson, 1969). Crary, et. al. (1962) found that this density was reached at depths ranging from about 9 m to 14 m at various sites on the Ross Ice Shelf. At depths below that at which this density is attained, densification proceeds at a decreasing rate by

recrystallization until permeability is reduced to zero at a density of about  $0.85 \text{ gm cm}^{-3}$  (Paterson, 1969). Below this level, density increases only very slowly with depth by compression of air bubbles in the ice (Shumskii, 1964; Paterson, 1969).

Seismic P-wave velocity has been shown experimentally to increase in direct proportion to ice density (Robin, 1958; Thiel and Ostenso, 1961; Kohnen and Bentley, 1973) (Figure 18). Kohnen and Bentley (1973) found that shear wave velocity at Byrd Station also appears to increase with density (Figure 19). The form of the velocity-depth increase in the Minna Bluff study area as described above is thus attributable to increasing density with depth. It is therefore concluded that the increase in P-wave and SH-wave velocity to a depth of about 37 m results from snow densification.

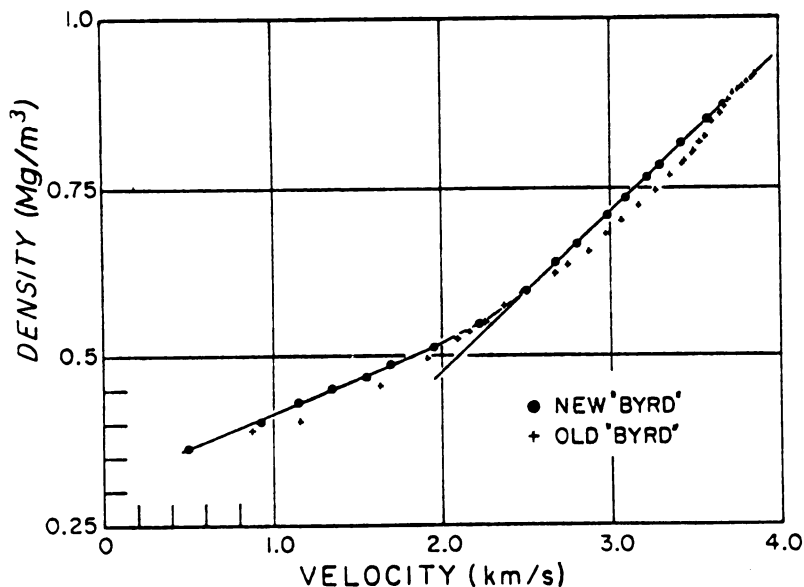


Figure 18. Density vs P-wave velocity, linear plot, at Byrd Station (From Kohnen and Bentley, 1973).

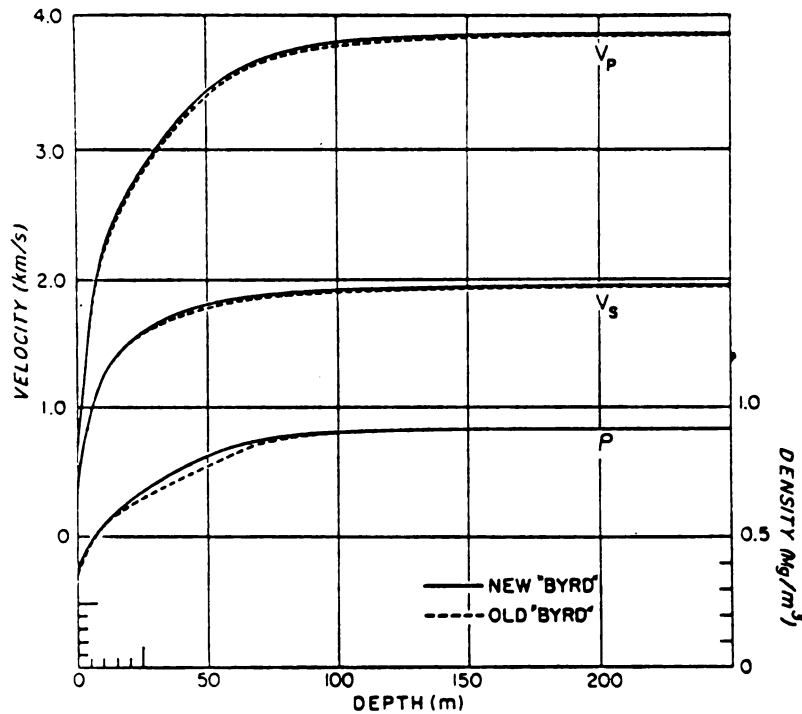
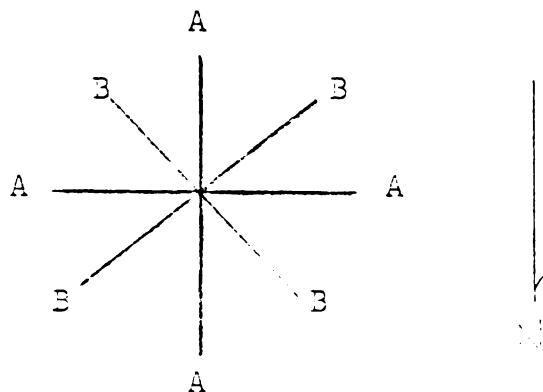


Figure 19. P-wave and S-wave velocities and densities vs depth at Byrd Station (From Kohnen & Bently, 1973).

#### B. VELOCITY INCREASE 37 M TO 70 M DEPTH: CRYSTAL FABRIC

The distribution of shear wave maximum velocity with depth and direction in the study area is strongly bimodal as observed above. The velocity-depth distribution is also centro-symmetric (Figure 20). Centro-symmetry characterizes velocity distributions in anisotropic media (Musgrave, 1970).

(Figure 20.)



Hexagonal ice crystals exhibit transverse isotropy (Appendix A), with the c crystallographic axis parallel to the axis of elastic symmetry (Bennett, 1968).

In an investigation of ultrasonic wave propagation in ice, Bennett (1968) found that, in a single ice crystal, the shear wave with particle motion in the plane containing the c-axis exhibits maximum velocity ( $2185 \text{ ms}^{-1}$ ) for propagation at an angle of  $45.5^\circ$  to the c-axis, with minimum velocity ( $1827 \text{ ms}^{-1}$ ) occurring for propagation in the direction of the c-axis. This is a variation of 18% of the mean velocity. The shear wave having direction of particle motion normal to the c-axis exhibits maximum velocity ( $1940 \text{ ms}^{-1}$ ) for propagation normal to the c-axis, with minimum velocity ( $1827 \text{ ms}^{-1}$ ) occurring for propagation in the direction of the c-axis, a variation of 6% of the mean velocity. Since the c-axis is the vertical axis in the standard crystallographic orientation, the shear wave with direction of particle motion in the plane containing the c-axis is an SV-wave, and the shear wave having direction of particle motion normal to this plane is a SH-wave.

Laboratory and field investigations of ice petrofabrics under conditions of known shear stress, as discussed in Chapter 1, show that ice crystal c-axes tend to reorient normal to the direction of applied shear stress with basal planes aligned parallel to shear stress. The average maximum velocities for the two shear wave sets,  $1830 \text{ ms}^{-1}$  and  $2056 \text{ ms}^{-1}$ , differ by 11.6%. From Bennett's results stated above, if the

ice in the study area exhibits an aggregate c-axis alignment, then direction of particle motion for the two shear wave velocity sets is inferred to be in the plane containing the c-axes. Further, since minimum shear wave velocity for single ice crystals (above) occurs along and perpendicular to the c-axis, the distribution of SH-wave maximum velocity about the array implies an aggregate horizontal East-West or North-South c-axis orientation, with vertical basal planes oriented North-South or East-West, respectively. It is concluded, from the petrofabric results cited above and the direction of shear stress as inferred in Chapters 1 and 2, that the probable c-axis orientation is East-West.

The maximum shear wave velocity in the study area ( $2056 \text{ ms}^{-1}$ ) is significantly greater than that determined by Bennett (1968) for pure isotropic ice ( $1940 \text{ ms}^{-1}$ ). The minimum velocity for shear wave propagation in a single ice crystal with particle motion in the plane of the c-axis ( $1827 \text{ ms}^{-1}$ ), as stated above, is virtually identical to the Set A shear wave maximum velocity ( $1830 \text{ ms}^{-1}$ ). Therefore, it is further concluded that velocity anisotropy resulting from aggregate c-axis alignment, as presented in the above discussion, is primarily responsible for the observed shear wave velocity distribution from 37 m to 70 m depth.

### C. HETEROGENIETY IN THE NEAR SURFACE

The error in both velocity and depth determination for compressional and shear waves (Figure 13 and Table 3) appears

excessively large above 20 m, and increases towards the surface. Vertical inhomogeneity in the near surface layers of the Ross Ice Shelf, as evidenced by the discontinuous nature of the overall density increase with depth, has been noted by Crary, et. al., (1962). P-wave and SH-wave velocities at the surface were observed to range from about  $287 \text{ ms}^{-1}$  to  $364 \text{ ms}^{-1}$ , and  $612 \text{ ms}^{-1}$  to  $1172 \text{ ms}^{-1}$ , respectively, in this study (Table III). Thus, it is concluded that areal heterogeneity is also important in the near surface layers of the ice shelf. Furthermore, the large error estimates noted above are thus largely attributable to areal heterogeneity in the layers above 20 m depth.

#### D. P-WAVE VELOCITIES AFFECTED BY FRACTURING

Maximum P-wave velocity in the study area was found to be about  $3671 \text{ ms}^{-1}$  (Chapter 4). Bennett (1968) found that compressional wave velocity for a single ice crystal varied with propagation direction from  $3803 \text{ ms}^{-1}$  to  $4077 \text{ ms}^{-1}$ . Crary, et. al. (1962), found the maximum P-wave velocity in various areas of the Ross Ice Shelf to range from about  $3750 \text{ ms}^{-1}$  to  $3814 \text{ ms}^{-1}$ , with an average maximum velocity of about  $3780 \text{ ms}^{-1}$ . Thus, maximum P-wave velocity observed near Minna Bluff is abnormally low.

However, the velocity at 37 m depth is about 5% to 10% higher than that reported elsewhere on the ice shelf at this depth. This implies that density is unusually high at 37 m depth. At Little America V, the density at 37 m is about  $0.7 \text{ gm cm}^{-3}$  (Figure 6), well within the firn zone



(Paterson, 1969). The bimodal maximum shear wave velocity distribution observed in this study has a mean of  $1943 \text{ ms}^{-1}$ , very close to the isotropic shear wave velocity of pure ice ( $1940 \text{ ms}^{-1}$ ) (Bennett, 1968). Since maximum velocity for both the P-waves and Set A of the SH-waves, as discussed above, is reached at about 37 m depth, it is inferred that bubbly ice of at least normal glacial ice density ( $\geq 0.85 \text{ gm cm}^{-3}$ , Paterson, 1969) is present at this level. Furthermore, the average maximum P-wave velocity is  $3671 \text{ ms}^{-1}$  in the study area (Chapter IV). This corresponds to a density of  $0.85 \text{ gm cm}^{-3}$  on the P-wave velocity-density curves given in Robin (1958).

The pattern of the isopachs of Figure 4 suggests that the major source of the ice in the Minna Bluff vicinity is Byrd Glacier. As observed above, bubbly ice rather than firn is believed to be present at about 37 m depth in the study area. At this depth, P-wave velocities are high relative to other locations on the ice shelf, as noted above. Shear wave velocities also are somewhat high near Minna Bluff, being about 2% higher than most other areas at 37 m depth, and about 7% higher at 70 m depth, as discussed below. Therefore, it is proposed that to a depth of approximately 37 m, the velocity increase reflects normal densification of snow accumulation, as discussed above. Below 37 m the unusually high velocities in the study area may be explained by the presence of dense glacial ice derived from the Byrd Glacier.

Fractures were observed at the surface in the vicinity of the study area (Chapter 2). One seismic effect of small fractures oriented randomly within a rock mass is to isotropically reduce the velocities from those of the unfractured rock (Crampin, McGonigle, and Bamford, 1980). If a zone of very fine fractures, which might be termed microcrevasses, was present in the ice below about 37 m, it is conceivable that the effect on seismic wave propagation through the fractured zone could be to both reduce the velocity and lengthen travel paths, thus resulting in a lower maximum velocity as observed at the surface. It should be recalled that the observed maximum P-wave velocity ( $3671 \text{ ms}^{-1}$ ) is low compared to maximum velocity in pure ice and in other areas of the ice shelf, as noted above. Thus, true maximum P-wave velocity has probably not been reached. Fracturing at depth could also be the reason why anisotropy was not observed in the P-wave studies. Crevasses are known to close with depth in the Ross Ice Shelf (H. Bennett, Personal communication). If the inferred micro-crevasse zone also closes with depth, then higher velocities, and perhaps anisotropy in the deeper layers, might be observed with a sufficiently long refraction profile. The SH-waves were apparently not affected by the proposed fracture zone. This suggests that the zone may consist of dry fractures, since if a water saturated fracture zone were present, a reduction of shear wave velocity, along with possible severe attenuation, might be anticipated. Several crevasses 5 km West of the study area were entered by the field party and found to be dry

(H. Bennett, Personal communications).

#### PROPOSED MODEL FOR THE MINNA BLUFF STUDY AREA

In the model developed in the above discussion, the increase of velocity with depth in the first 37 m is attributed to densification. The increase in shear wave velocity from 37 m to 70 m depth results from increased preferred orientation of c-axes. In the study area, a strong fabric is developed below 37 m, with c-axes oriented horizontally East-West, and basal planes vertical with North-South orientation. Areal and vertical heterogeneity characterize the near surface layers above 20 m depth. At 37 m, density and velocity appear to be abnormally high. This is attributed to a possible dense layer of glacial ice originating in the Byrd Glacier. A dry microcrevasse zone may exist in the glacial ice layer, explaining why P-wave maximum velocity was probably not reached.

#### COMPARISON OF VELOCITY-DEPTH PROFILES NEAR MINNA BLUFF WITH OTHER STUDIES

Crary, et. al. (1962), obtained velocity-depth profiles at various stations along the IGY traverse routes. P-wave profiles for Stations 14 and 58 (see map, Figure 3) are plotted in Figure 22, along with shear wave profiles at Station 58 and at Little America. P-wave profiles at Little America V, Byrd Station, and Ellsworth appear in Figure 21.

Comparison of these to Figures 14-17 indicate that to the common depth of sampling shear wave velocities are

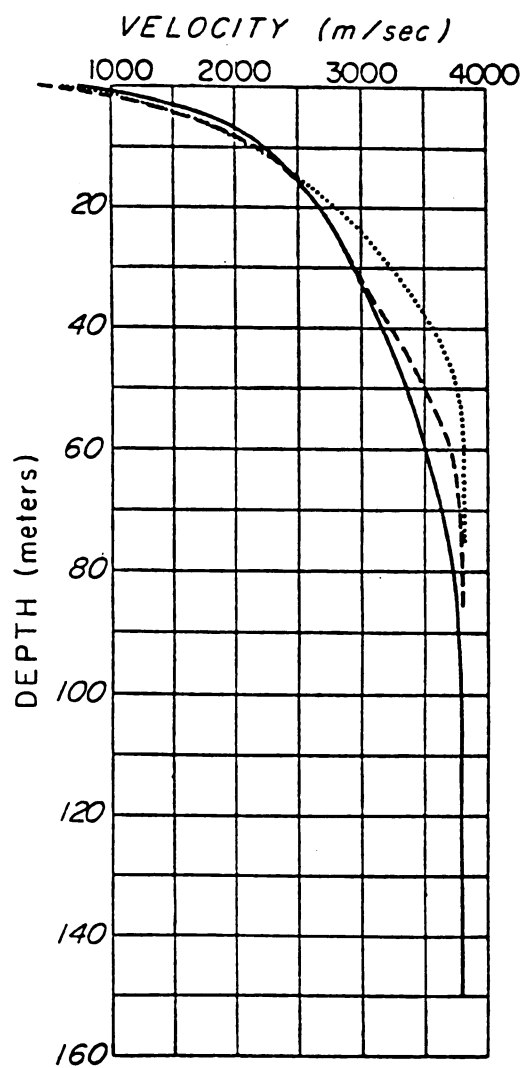


Figure 21. Velocity-Depth Profiles at Byrd (solid line), at Little America V. (dashed line), and at Ellsworth (dotted line).

similar in most areas. Compared to the profile at Little America Station (Figure 22), shear wave velocity increases somewhat more rapidly after 37 m near Minna Bluff, being about 7% greater at the 70 m depth. This is interpreted as reflecting the influence of crystal fabric and, possibly, dense glacial ice in the study area, as discussed above. P-wave velocities appear similar at all other sites on the Ross Ice Shelf to about 30 m depth, increasing more rapidly thereafter in the study area. At 37 m depth, velocity near Minna Bluff is in general 5% to 10% greater than elsewhere, even though maximum P-wave velocity as determined in this study is abnormally low, as compared with pure ice. The difference observed between V-Z profiles in different areas are thus attributed to differences in density structure, fracturing, and crystal orientation, as suggested by the above model.

#### IMPORTANCE OF SHEAR WAVES IN SEISMIC ANISOTROPY STUDIES

Bennett (1968, 1972) found P-waves to be affected less strongly by crystal fabric than shear waves, as noted in Chapter 1, for conic distributions of c-axes. For single ice crystals, he also found the variation of velocity with direction to be only about 7% for P-waves, versus as much as 18% for shear waves. Hence, it would be expected for shear waves to be better indicators of anisotropy than P-waves. The results of the present study tend to confirm this conclusion. It is also noted that shear waves may be characterized by better propagation in dry fractured zones than P-waves.

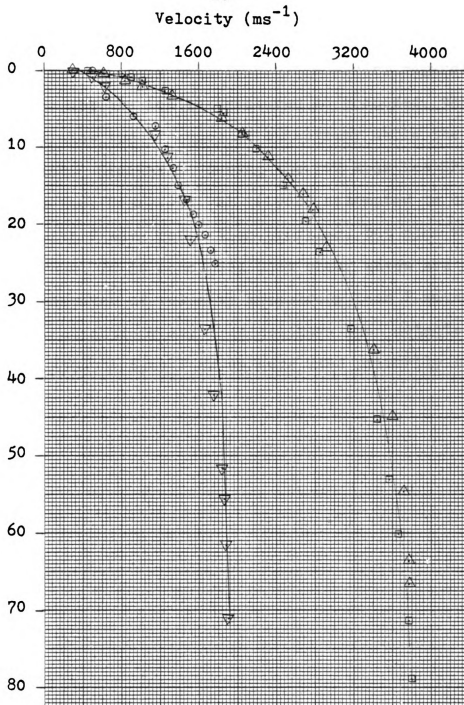


Figure 22: Ross Ice Shelf P and SH-wave Velocity-Depth Profiles.

P-waves                      IGY Traverse Station 14  
                                  IGY Traverse Station 58

SH-waves                    IGY Traverse Station 14  
                                  Little America Station

(Data from Crary, et. al., 1962)

Of course, the presence of such a fracture zone in the study area is not conclusively established. However, regardless of whether or not the ice is fractured as proposed, the shear wave results show the presence of anisotropy while the P-wave results do not. Similarly, during the IGY Ross Ice Shelf traverse studies, Crary, et. al. (1962) attempted to detect anisotropy with P-wave refraction profiles, but none was detected. Thus, it is concluded that shear waves are a more important indicator of velocity anisotropy than P-waves. Furthermore, anisotropy may thus not have been detected in previous studies because P-waves were used primarily or exclusively.

## APPENDICES



APPENDIX A

## APPENDIX A

### TRANSVERSE ISOTROPY

The following brief discussion of transverse isotropy is based primarily on Postma, 1957.

A medium in which the elastic properties are symmetrical with respect to a fixed axis is termed transversely isotropic. Since in the case of ice and other hexagonal crystals this axis parallels the c crystallographic axis, the c-axis will be presumed to correspond with the z-axis, defined above as the fixed axis of symmetry, in the ensuing discussion.

Hooke's law (Love, 1934) may be stated in matrix form as follows:

$$\begin{bmatrix} c_{11} & c_{12} & c_{13} & c_{14} & c_{15} & c_{16} \\ c_{21} & c_{22} & c_{23} & c_{24} & c_{25} & c_{26} \\ c_{31} & c_{32} & c_{33} & c_{34} & c_{35} & c_{36} \\ c_{41} & c_{42} & c_{43} & c_{44} & c_{45} & c_{46} \\ c_{51} & c_{52} & c_{53} & c_{54} & c_{55} & c_{56} \\ c_{61} & c_{62} & c_{63} & c_{64} & c_{65} & c_{66} \end{bmatrix} \begin{bmatrix} e_{xx} \\ e_{yy} \\ e_{zz} \\ e_{yz} \\ e_{zx} \\ e_{xy} \end{bmatrix} = \begin{bmatrix} X_x \\ Y_y \\ Z_z \\ Y_z \\ Z_x \\ X_y \end{bmatrix} \quad (1)$$

in which:

$$c_{ij} = c_{ji} (i, j = 1, \dots, 6)$$

$X_x$  = normal component of traction across a surface element perpendicular to the x-axis, etc.

$Y_z$  = tangential component of traction parallel to the y-axis across a surface element perpendicular to the z-axis, etc.

$$e_{xx} = \frac{\partial u}{\partial x}; \quad e_{yy} = \frac{\partial v}{\partial y}; \quad e_{zz} = \frac{\partial w}{\partial z};$$

$$e_{yz} = \frac{\partial w}{\partial y} + \frac{\partial v}{\partial z}; \quad e_{zx} = \frac{\partial u}{\partial z} + \frac{\partial w}{\partial x}; \quad e_{xy} = \frac{\partial v}{\partial x} + \frac{\partial u}{\partial y}$$

where  $u, v, w$  are the components of the displacement,  $e_{xx}$  is the linear dilation of line elements in the  $z$ -axis direction in the unstrained state, and  $e_{yz}$  is the decrease of the angle between the two line elements which are parallel to the  $y$  and  $z$  axes in the unstrained state. Note that  $Y_z = Z_y$  (Love, 1934).

With the  $z$ -axis as the axis of symmetry, and assuming the validity of (1), the coefficients  $c_{ij}$  in (1) must be invariant under rotations about the  $z$ -axis. Therefore (1) becomes (Love, 1934):

$$\begin{bmatrix} c_{11} & c_{12} & c_{13} & 0 & 0 & 0 \\ c_{12} & c_{11} & c_{13} & 0 & 0 & 0 \\ c_{13} & c_{13} & c_{33} & 0 & 0 & 0 \\ 0 & 0 & 0 & c_{44} & 0 & 0 \\ 0 & 0 & 0 & 0 & c_{44} & 0 \\ 0 & 0 & 0 & 0 & 0 & \frac{c_{11}-c_{12}}{2} \end{bmatrix} \begin{bmatrix} e_{xx} \\ e_{yy} \\ e_{zz} \\ e_{yz} \\ e_{zx} \\ e_{xy} \end{bmatrix} = \begin{bmatrix} X_x \\ Y_y \\ Z_z \\ Y_z \\ Z_x \\ X_y \end{bmatrix} \quad (2)$$

There are thus five independent coefficients ( $c_{11}, c_{12}, c_{13}, c_{33}, c_{44}$ ) in the case of transversely isotropic media.

The propagation of plane waves in transversely isotropic media will now be briefly considered. The equations of motion are:

$$\begin{aligned} \frac{\partial X_x}{\partial x} + \frac{\partial X_y}{\partial y} + \frac{\partial X_z}{\partial z} &= d \frac{\partial^2 u}{\partial t^2} \\ \frac{\partial Y_x}{\partial x} + \frac{\partial Y_y}{\partial y} + \frac{\partial Y_z}{\partial z} &= d \frac{\partial^2 v}{\partial t^2} \\ \frac{\partial Z_x}{\partial x} + \frac{\partial Z_y}{\partial y} + \frac{\partial Z_z}{\partial z} &= d \frac{\partial^2 w}{\partial t^2} \end{aligned} \quad (3)$$

where  $d$  = density.

Substituting (2) into (3):

$$\begin{aligned}
& c_{11} \frac{\partial^2 u}{\partial x^2} + c_{66} \frac{\partial^2 u}{\partial y^2} + c_{44} \frac{\partial^2 u}{\partial z^2} + (c_{11} - c_{66}) \frac{\partial^2 v}{\partial x \partial y} + (c_{13} + c_{44}) \frac{\partial^2 w}{\partial x \partial z} \\
& \qquad \qquad \qquad = d \frac{\partial^2 u}{\partial t^2} \\
& (c_{11} - c_{66}) \frac{\partial^2 u}{\partial x \partial y} + c_{66} \frac{\partial^2 v}{\partial x^2} + c_{11} \frac{\partial^2 v}{\partial y^2} + c_{44} \frac{\partial^2 v}{\partial z^2} + (c_{13} + c_{44}) \frac{\partial^2 w}{\partial y \partial z} \\
& \qquad \qquad \qquad = d \frac{\partial^2 v}{\partial t^2} \quad (4) \\
& (c_{13} + c_{44}) \frac{\partial^2 u}{\partial x \partial z} + (c_{13} + c_{44}) \frac{\partial^2 v}{\partial y \partial z} + c_{44} \frac{\partial^2 w}{\partial x^2} + c_{44} \frac{\partial^2 w}{\partial y^2} + c_{33} \frac{\partial^2 w}{\partial z^2} \\
& \qquad \qquad \qquad = d \frac{\partial^2 w}{\partial t^2}
\end{aligned}$$

For the plane wave case, considering because of the symmetry only waves normal to the  $y = 0$  plane, equations of the following form describe the wave motion:

$$\begin{aligned}
u &= u_0 f(x \cos \theta + z \sin \theta - Vt) \\
v &= v_0 f(x \cos \theta + z \sin \theta - Vt) \\
w &= w_0 f(x \cos \theta + z \sin \theta - Vt)
\end{aligned} \quad (5)$$

where  $f$  may be an arbitrary function of its argument.

Substituting (5) into (4) and noting that all terms in (4) containing  $\partial/\partial y$  are zero for this case:

$$\begin{aligned}
(c_{11} \cos^2 \theta + c_{44} \sin^2 \theta) u_0 + (c_{13} + c_{44}) \sin \theta \cos \theta w_0 &= dV^2 u_0 \\
(c_{66} \cos^2 \theta + c_{44} \sin^2 \theta) v_0 &= dV^2 v_0 \\
(c_{13} + c_{44}) \sin \theta \cos \theta u_0 + (c_{44} \cos^2 \theta + c_{33} \sin^2 \theta) w_0 &= dV^2 w_0
\end{aligned} \quad (6)$$

Where  $dV^2 = c_{66} \cos^2 \theta + c_{44} \sin^2 \theta$ , one solution of (6) is  $u_0 = w_0 = 0$ , with  $v_0$  arbitrary. This is the case of a plane

wave having direction of particle motion normal to the  $y = 0$  plane which, due to the symmetry, typifies any meridional plane.

For  $\phi = 0$ ,  $V_3(0) = \sqrt{c_{66}/d}$ ; for  $\phi = \pi/2$ ,  $V_3(\pi/2) = \sqrt{c_{44}/d}$ .

For all values of  $\phi$  ( $\phi = 0$  to  $\phi = 2\pi$ ), the wavefront envelope at  $t = 1$  is the ellipse

$$\frac{x^2}{c_{66}/d} + \frac{z^2}{c_{44}/d} = 1 \quad (7)$$

The ellipsoid formed by revolution about the  $z$ -axis of (7) is the wave surface (Love, 1934).

Other solutions, where  $v_0 = 0$ ,  $u_0 \neq 0$ ,  $w_0 \neq 0$ , exist when

$$\begin{aligned} c_{11}\cos^2\phi + c_{44}\sin^2\phi - dV^2 & \quad (c_{13} + c_{44})\sin\phi\cos\phi \\ (c_{13} + c_{44})\sin\phi\cos\phi & \quad c_{44}\cos^2\phi + c_{33}\sin^2\phi - dV^2 = 0 \end{aligned} \quad (8)$$

These solutions correspond to plane waves having direction of particle motion within the  $y = 0$  plane.

Applying the substitutions:

$$\begin{aligned} c_{11}\cos^2\phi + c_{44}\sin^2\phi &= a & (c_{13} + c_{44})\sin\phi\cos\phi &= b \\ c_{44}\cos^2\phi + c_{33}\sin^2\phi &= c & dV^2 &= R \\ w_0/u_0 &= \tan\theta \end{aligned}$$

the first and third equations of (6) assume the form

$$\begin{aligned} a + b\tan\theta &= R \\ b + c\tan\theta &= R\tan\theta \end{aligned} \quad (9)$$

where  $\theta$  is the direction of particle displacement. Eliminating  $\theta$ :

$$\frac{R - a}{b} = \frac{b}{R - c} \quad (10)$$

Eliminating R:

$$\begin{aligned} \tan\theta(a + b\tan\theta) &= b + c\tan\theta \\ \tan 2\theta &= \frac{2\tan\theta}{1 - \tan^2\theta} = \frac{2b}{a - c} \end{aligned} \quad (11)$$

These equations may be solved graphically (see Postma, 1955, for details) yielding:

$$\begin{aligned} \varnothing = 0: R_1 &= c_{11}, \theta = 0; R_2 = c_{44}, \theta = \pi/2 \\ V_1 &= \sqrt{c_{11}/d}; \quad V_2 = \sqrt{c_{44}/d} \\ \varnothing = \pi/2: R_1 &= c_{33}, \theta = \pi/2; R_2 = c_{44}, \theta = \pi \\ V_1 &= \sqrt{c_{33}/d}; \quad V_2 = \sqrt{c_{44}/d} \end{aligned}$$

where  $R_1$  and  $R_2$  are the roots of the quadratic equation (10) and  $R_1 > R_2$ .

Therefore, the wave having the largest normal velocity resembles a p-wave, and the slower wave resembles a shear wave. In the  $\varnothing = 0$  and  $\varnothing = \pi/2$  directions the waves are purely longitudinal or purely transverse, but not in other directions in general.

## APPENDIX B

## APPENDIX E

### DERIVATION OF WEICHERT-HERGLOTZ-BATEMAN INTEGRAL

The following derivation is outlined in Officer (1958).

Let velocity be assumed to increase as a continuous function of depth, e.g. Figure 23:

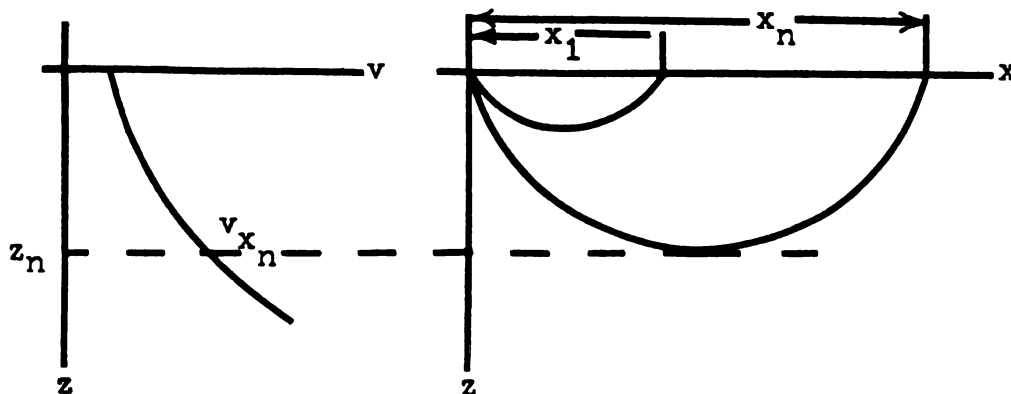


Figure 23.

Then both the horizontal range  $x$  along a given ray path, say  $x_n$ , and the travel time  $t$  can be expressed parametrically in terms of depth  $z$  and angle of inclination  $\theta$  as follows (Figure 24):

$$x_n = \int_0^{z_n} \tan \theta \, dz \quad (1)$$

$$t = \int_0^s \frac{ds}{v} = \int_0^{z_n} \frac{dz}{v \cos \theta} \quad (2)$$

The ray parameter  $p$  is defined as

$$p = \frac{\sin \theta}{v(z)}, \quad \therefore \sin \theta = pv(z)$$

For  $\sin x = a$ ,  $\tan x = \frac{a}{(1-a^2)^{\frac{1}{2}}}$ ,  $\cos x = (1-a^2)^{\frac{1}{2}}$ , hence

$$\tan \theta = \frac{pv(z)}{(1-p^2v^2(z))^{\frac{1}{2}}} \quad (3)$$



$$\cos \theta = (1-p^2v^2)^{\frac{1}{2}} \quad (4)$$

Substituting (3) and (4) in (1) and (2), respectively,

$$x = \int_0^z \frac{pvdz}{(1-p^2v^2)^{\frac{1}{2}}}$$

$$t = \int_0^z \frac{dz}{v(1-p^2v^2)^{\frac{1}{2}}}$$

Rearranging,

$$x = p \int_0^z \frac{vdz}{v(1/v^2-p^2)^{\frac{1}{2}}} \quad (5)$$

$$t = \int_0^z \frac{dz}{v^2(1/v^2-p^2)^{\frac{1}{2}}} \quad (6)$$

Defining  $\mu = 1/v$ , and substituting in (5) and (6),

$$x = p \int_0^z \frac{dz}{(\mu^2-p^2)^{\frac{1}{2}}} \quad (7)$$

$$t = \int_0^z \frac{\mu^2 dz}{(\mu^2-p^2)^{\frac{1}{2}}} \quad (8)$$

Assume that the ray under discussion returns to the source depth. The horizontal range  $x_n$  and the travel time  $t$  are therefore:

$$x_n = 2p \int_0^{z_n} \frac{dz}{(\mu^2-p^2)^{\frac{1}{2}}} \quad (9)$$

$$t = 2 \int_0^{z_n} \frac{\mu^2 dz}{(\mu^2-p^2)^{\frac{1}{2}}} \quad (10)$$

where  $z_n$  is the depth of maximum penetration of the ray path.

Let two adjacent rays, penetrating to some depth  $z$ , be defined by ray parameters  $p$  and  $p+dp$ . Draw wave surfaces  $S_1$  and  $S_2$  normal to them (Figure 24).  $S_1$  and  $S_2$  will be separated by range interval  $dx$  and time interval  $dt$ .

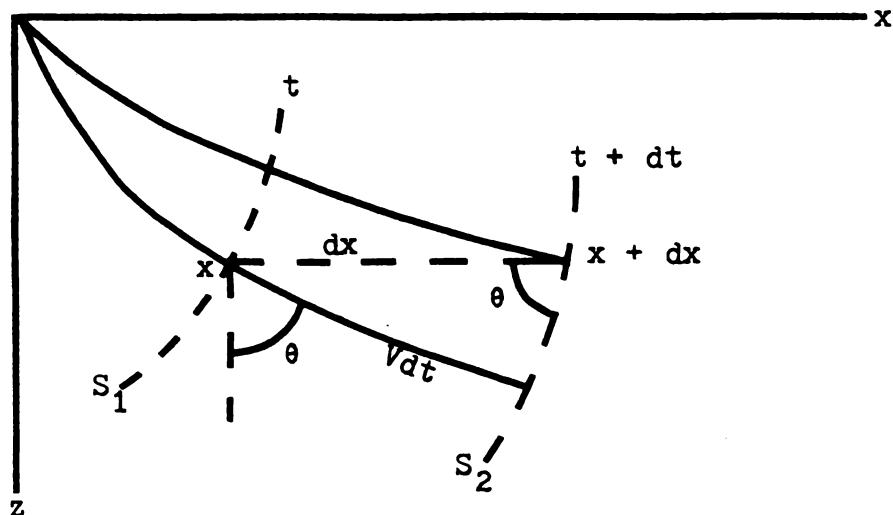


Figure 24.

From Figure 24,

$$\sin \theta = \frac{v dt}{dx}$$

But:  $\sin \theta = pv$ ,  $\therefore$

$$p = \frac{dt}{dx} = \frac{1}{v}$$

Since  $\theta = \frac{\pi}{2} = \theta_{x_i}$  at the vertex of a given ray, where

$v = v_{x_i}$ ,

$$p = \frac{1}{v_{x_i}}, \text{ or} \quad (11)$$

$$p = \mu_{x_i}$$

Note that  $v_{x_i}$ , attained at the depth of maximum penetration  $z_i$ , is the greatest velocity reached along the ray path. A ray emergent at horizontal range  $x_i$  will exhibit the same angle of inclination that it had at the source, since, from Snell's Law

$$\frac{\sin \theta_0}{v_0} = \frac{\sin \theta}{v} = p \quad (12)$$

The reciprocal slope of the T-X curve at  $x_i$  is the velocity  $\bar{v}$  with which the associated wave front travels along the surface  $z = 0$ . Referring to Figure 25,

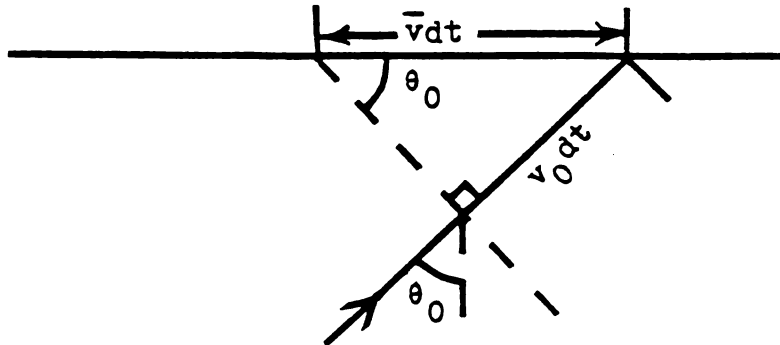


Figure 25.

$$\sin \theta_0 = \frac{v_0 dt}{\bar{v} dt}$$

$$\bar{v} = \frac{v_0}{\sin \theta_0}$$

Referring to Equations (11) and (12),  $\therefore$

$$\bar{v} = v_{x_i}$$

Hence, the reciprocal slope of the T-X curve at  $x_i$  is the velocity at the depth of maximum penetration for the ray emergent at  $x_i$  (Figure 26).

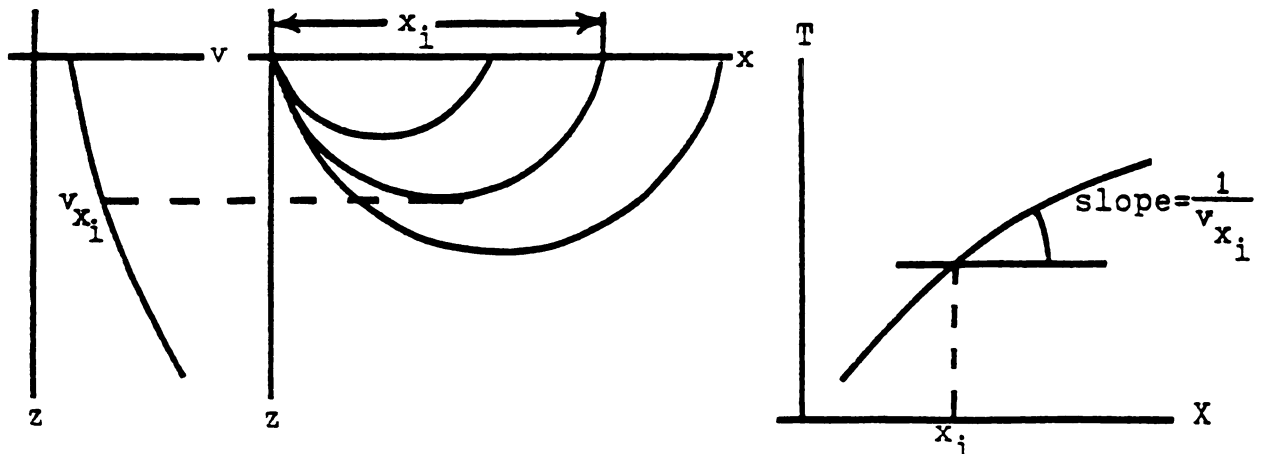


Figure 26.

Equation (9) may be rewritten as an integration along the ray path as follows:

$$x = 2p \int_{\mu_0}^{\mu_{x_n}} \frac{(dz/du) du}{(\mu^2 - p^2)^{\frac{1}{2}}}$$

Applying the operator  $\int_{p_0}^{p_{x_n}} (p^2 - \mu_{x_n}^2)^{-\frac{1}{2}} dp$  to both sides:

$$\int_{\mu_0}^{\mu_{x_n}} \frac{x dp}{(p^2 - \mu_{x_n}^2)^{\frac{1}{2}}} = \int_{\mu_0}^{\mu_{x_n}} dp \int_{\mu}^{\mu_{x_n}} \frac{2p (dz/du) du}{(p^2 - \mu_{x_n}^2)^{\frac{1}{2}} (\mu^2 - p^2)^{\frac{1}{2}}} \quad (13)$$

This operation is an integration across the rays from the ray at  $x = 0$  to the ray at  $x_n$  whose vertex is at a depth where  $v_{x_n} = 1/\mu_{x_n}$ . The integration limits have the relation:

$$p_0 = \mu p_0 = \mu_0 = 1/v_0$$

$$p_{x_n} = \mu p_{x_n} = \mu_{x_n} = 1/v_{x_n}$$

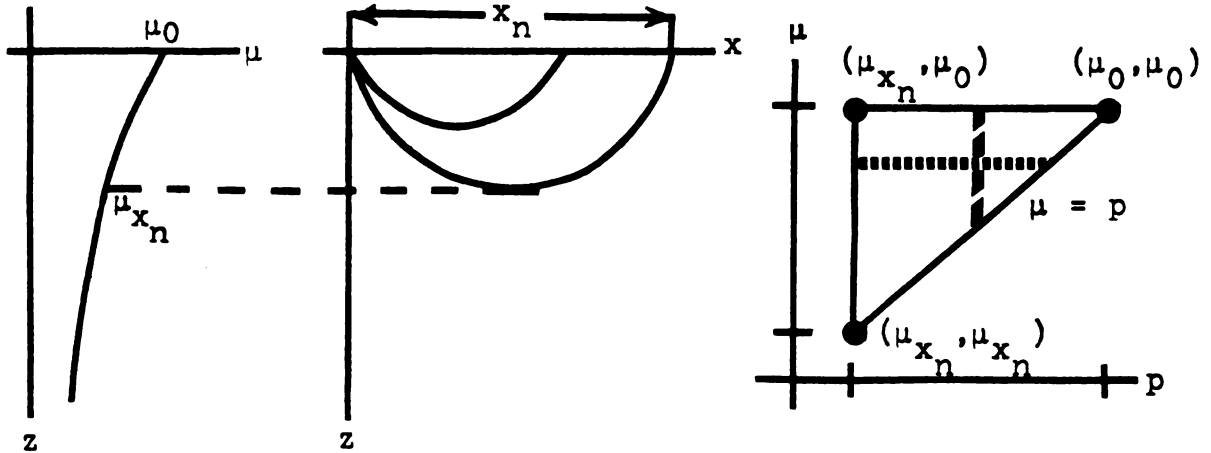


Figure 27.

Referring to Figure 27, the order and limits of integration of (13) may be readily changed to the following:

$$\int_{\mu_0}^{\mu_{x_n}} \frac{x dp}{(p^2 - \mu_{x_n}^2)^{\frac{1}{2}}} = \int_{\mu_0}^{\mu_{x_n}} d\mu \int_{\mu}^{\mu_{x_n}} \frac{(dz/du) 2p dp}{p(-p^4 + (\mu^2 + \mu_{x_n}^2) p^2 - \mu_{x_n}^2 \mu^2)^{\frac{1}{2}}} \quad (14)$$

Observing that, for the integral on the left-hand side:

$$\int_{\mu_0}^{\mu_{x_n}} \frac{x dp}{(p^2 - \mu_{x_n}^2)^{\frac{1}{2}}} = \int_{\mu_0}^{\mu_{x_n}} \frac{x}{(p^2/\mu_{x_n}^2 - 1)^{\frac{1}{2}}} \frac{dp}{\mu_{x_n}}$$

$$\int_{\mu_0}^{\mu_{x_n}} \frac{x dp}{(p^2 - \mu_{x_n}^2)^{\frac{1}{2}}} = \int_{\mu_0}^{\mu_{x_n}} x \left( \frac{p^2}{\mu_{x_n}^2} - 1 \right)^{-\frac{1}{2}} \frac{dp}{\mu_{x_n}} \quad (15)$$

Since  $\text{dcosh}^{-1}(z) = (z^2 - 1)^{-\frac{1}{2}} dz$ , where  $z = p/\mu_{x_n}$ , the integral on the right of (15) is of the form  $\int u dv$ , where  $v = \cosh^{-1}(p/\mu_{x_n})$ . It is readily seen that the integral may be evaluated by parts, since  $\int u dv = uv - \int v du + c$ .

Hence:

$$\int_{\mu_0}^{\mu_{x_n}} \frac{x dp}{(p^2 - \mu_{x_n}^2)^{\frac{1}{2}}} = x \cosh^{-1}\left(\frac{p}{\mu_{x_n}}\right) \frac{\mu_{x_n}}{\mu_0} - \int_{\mu_0}^{\mu_{x_n}} \frac{dx}{dp} \cosh^{-1}\left(\frac{p}{\mu_{x_n}}\right) dp \quad (16)$$

Evaluating the first term on the right of (16):

$$\begin{aligned} x \cosh^{-1}\left(\frac{p}{\mu_{x_n}}\right) \frac{\mu_{x_n}}{\mu_0} &= x \cosh^{-1}\left(\frac{\mu_{x_n}}{\mu_{x_n}}\right) - x \cosh^{-1}\left(\frac{\mu_0}{\mu_{x_n}}\right) \\ &= x \cosh^{-1}(1) - x \cosh^{-1}\left(\frac{\mu_0}{\mu_{x_n}}\right) \\ &= -x \cosh^{-1}\left(\frac{\mu_0}{\mu_{x_n}}\right) \end{aligned}$$

Observing that when  $p = \mu_0$ ,  $x = 0$ ,

$$x \cosh^{-1}\left(\frac{p}{\mu_{x_n}}\right) \frac{\mu_{x_n}}{\mu_0} = 0$$

Thus,

$$\int_{\mu_0}^{\mu_{x_n}} \frac{x dp}{(p^2 - \mu_{x_n}^2)^{\frac{1}{2}}} = - \int_{\mu_0}^{\mu_{x_n}} \frac{dx}{dp} \cosh^{-1}\left(\frac{p}{\mu_{x_n}}\right) dp \quad (17)$$

Referring to the first integral on the right side of (14):

$$\int_{\mu}^{\mu_{x_n}} \frac{(dz/d\mu) 2p dp}{(-p^4 + (\mu^2 + \mu_{x_n}^2) p^2 - \mu_{x_n}^2 \mu^2)^{\frac{1}{2}}} = \frac{dz}{d\mu} \int_{\mu}^{\mu_{x_n}} \frac{2p dp}{(-p^4 + (\mu^2 + \mu_{x_n}^2) p^2 - \mu_{x_n}^2 \mu^2)^{\frac{1}{2}}}$$

Letting  $a = -\mu_{x_n}^2 \mu^2$ ,  $b = \mu^2 + \mu_{x_n}^2$ ,  $c = -1$ ,  $u = p^2$ , it is readily seen that the integral on the right above is of the form:

$$\int \frac{du}{(a + bu + cu^2)^{\frac{1}{2}}} = (-c)^{-\frac{1}{2}} \sin^{-1} \left( \frac{-2cu - b}{(b^2 - 4ac)^{\frac{1}{2}}} \right), \quad c < 0$$

Thus:

$$\begin{aligned} \int_{\mu}^{\mu_{x_n}} \frac{2p dp}{(-\mu_{x_n}^2 \mu^2 + (\mu^2 + \mu_{x_n}^2) p^2 - p^4)^{\frac{1}{2}}} &= \frac{\sin^{-1} \left( \frac{-2(-1)(p^2) - (\mu^2 + \mu_{x_n}^2)}{((\mu^2 + \mu_{x_n}^2)^2 - 4(-\mu_{x_n}^2 \mu^2)(-1))^{\frac{1}{2}}} \right)}{(-(-1))^{\frac{1}{2}}} \mu_{x_n} \\ &= \sin^{-1} \left( \frac{2p^2 - (\mu^2 + \mu_{x_n}^2)}{(\mu^4 - 2\mu_{x_n}^2 \mu^2 + \mu_{x_n}^4)^{\frac{1}{2}}} \right) \mu_{x_n} \\ &= \sin^{-1} \left( \frac{2p^2 - (\mu^2 + \mu_{x_n}^2)}{\mu^2 - \mu_{x_n}^2} \right) \mu_{x_n} \\ &= \sin^{-1} \left( \frac{2\mu_{x_n}^2 - \mu^2 - \mu_{x_n}^2}{\mu^2 - \mu_{x_n}^2} \right) - \sin^{-1} \left( \frac{2\mu^2 - \mu^2 - \mu_{x_n}^2}{\mu^2 - \mu_{x_n}^2} \right) \\ &= \sin^{-1} \left( \frac{-(\mu^2 - \mu_{x_n}^2)}{\mu^2 - \mu_{x_n}^2} \right) - \sin^{-1} \left( \frac{\mu^2 - \mu_{x_n}^2}{\mu^2 - \mu_{x_n}^2} \right) \\ &= \sin^{-1}(-1) - \sin^{-1}(1) \\ &= -\pi/2 - \pi/2 \\ &= -\pi \end{aligned}$$

Thus, the right side of (14) reduces to:

$$-\pi \int_{\mu_0}^{\mu_{x_n}} \frac{dz}{d\mu} d\mu$$

Therefore, referring to Equation (17):

$$\int_{\mu_0}^{\mu_{x_n}} \frac{dx}{dp} \cosh^{-1}\left(\frac{p}{\mu_{x_n}}\right) dp = \pi \int_{\mu_0}^{\mu_{x_n}} \frac{dz}{d\mu} d\mu$$

Or, since:

$$x = 0 \text{ at } p = \mu_0$$

$$x = x_n \text{ at } p = \mu_{x_n}$$

$$z = 0 \text{ at } \mu = \mu_0$$

$$z = z_n \text{ at } \mu = \mu_{x_n}$$

$$\int_0^{x_n} \cosh^{-1}\left(\frac{p}{\mu_{x_n}}\right) dx = \pi \int_0^{z_n} dz = \pi z_n$$

$$z_n = \frac{1}{\pi} \int_0^{x_n} \cosh^{-1}\left(\frac{p}{\mu_{x_n}}\right) dx$$

Or, since  $p = 1/v_{x_i}$  and  $\mu_{x_n} = 1/v_{x_n}$ ,

$$z_n = \frac{1}{\pi} \int_0^{x_n} \cosh^{-1}\left(\frac{v_{x_n}}{v_{x_i}}\right) dx \quad (18)$$

Equation (18) is known as the Weichert-Herglotz-Bateman (or W.H.B.) integral.

## APPENDIX C



## APPENDIX C

### SEISMIC EVENT RECOGNITION AND ARRIVAL TIME DETERMINATION

#### COMPRESSIONAL WAVES

On the P-wave records, recognition of the compressional wave arrival was generally simple, since it was the first visible seismic event, due to its greater velocity, and of high relative amplitude.

Each prepared seismic section consists of 26 traces. Traces 1 and 26 are used only to record the time break (the time of generation of the seismic signal). On each remaining trace is recorded the output with time of one of the 24 geophones of the array line. The time axes of all traces are parallel. The origin for the time axis of each trace, the zero time reference line, is therefore a line drawn through the time break normal to the time axes of all the geophone traces.

The arrival times of the first break and first peak of the wave train on each geophone trace were measured from the zero time reference line. Precision of measurement was  $\pm 0.2$  ms. Each first break time was then subtracted from the corresponding peak time, and the difference, being  $\frac{1}{4}$  the period, was averaged for all 24 traces. The result was then subtracted from the peak times to correct them to first arrival times. This procedure was used to reduce error in arrival time determination, since peak times can usually be determined to a much greater degree of precision than can

first break times due to the general lack of sharpness of the latter.

### SHEAR (SH) WAVES

Positive identification of SH-wave events was achieved due to the success of the mortar reversal technique described in Chapter 3. When a left-right pair of seismic sections are properly aligned and overlaid on a light table, SH-wave events are readily recognizable because of the opposite directions of motion recorded on corresponding traces (Figure 28). Since, all other factors being the same, the times recorded for each event should be identical on corresponding traces, the method following was employed to reduce error in SH arrival times. The first peak time on one trace was measured, as described above for P-waves, and averaged with the first trough time measured from the corresponding trace on the other section. The associated first break times were also measured and averaged. The resulting peak-trough average times were then treated as described above for P-wave peak times.

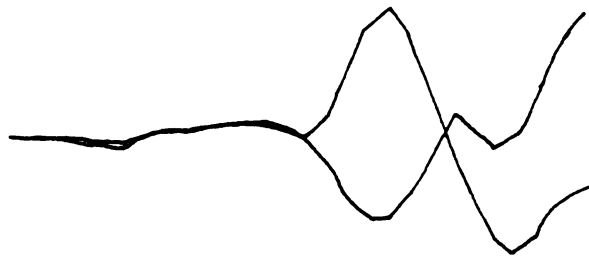


Figure 28. SH-Wave identification; sample of corresponding overlaid traces.

## APPENDIX D

# APPENDIX A

## SH-WAVE TIME-DISTANCE DATA\*

TABLE D-I

	(0°)	(180°)	(45°)	(225°)	(90°)	(270°)	(135°)	(315°)
	000	000	045	045	090	090	135	135
X	1D	1R	1D	1R	1D	1R	1D	1R
50	26.3	30.3	21.8	23.2	25.3	24.0	25.1	20.9
100	40.4	42.1	36.2	36.4	40.0	38.6	37.0	33.7
150	51.7	52.4	48.8	50.2	51.2	49.9	49.0	44.9
200	63.5	62.8	59.0	59.1	61.3	60.4	59.8	55.5
250	72.9	72.0	68.7	68.8	71.3	69.6	67.7	63.7
300	83.7	81.0	78.6	78.9	81.1	79.3	79.0	75.1
350	92.5	89.7	88.0	87.9	90.5	88.7	88.4	84.7
400	101.9	99.1	97.4	96.7	99.2	97.0	96.5	
450	110.7	107.8	106.3	105.7	108.0	106.4	105.1	102.1
500	119.4	116.9	114.5	115.1	117.3	115.7	115.1	111.7
550	127.8	125.5	123.1	123.2	125.8	123.9	124.3	119.9
600	136.5	134.0	132.1	130.6	134.3	132.3	131.8	128.3
650	144.3	143.2	139.7	141.2	141.2	141.6	138.8	138.5
700	152.7	151.7	148.3	148.0	150.0	150.4	147.5	146.1
750	161.0	160.4	156.3	157.0	158.9	159.2	156.0	153.9
800	169.3	168.3	164.3	164.6	166.5	166.5	163.0	161.5
850	177.3	176.5	172.2	172.6	170.2	174.9		169.7
900	185.5	185.0	180.0	181.6	184.6	183.7	179.0	178.3
950	194.3	193.1	188.0	188.4	192.0	191.5	187.1	185.3
1000	202.2	201.6	195.2	196.5	200.7	199.4	193.2	192.9
1050	211.1	209.9	203.7	204.5	209.0	208.0	203.9	201.1
1100	219.3	217.3	211.3	212.6	216.9	217.0	210.9	209.5
1150	228.0	224.9	219.2	218.8	226.0	225.3	219.0	216.5
1200	235.9	233.7	226.5	226.4	232.9	233.7	225.6	224.1

\* Distance in feet, time in milliseconds.

SH-WAVE TIME-DISTANCE DATA

	(0°)	(180°)	(45°)	(225°)	(90°)	(270°)	(135°)	(315°)
	000	000	045	045	090	090	135	135
<u>X</u>	<u>2D</u>	<u>2R</u>	<u>2D</u>	<u>2R</u>	<u>2D</u>	<u>2R</u>	<u>2D</u>	<u>2R</u>
1100	219.4	217.2	211.4	211.5	216.3	216.9	210.9	209.5
1150	227.8	225.6	219.2	219.3	224.1	226.0	218.2	216.7
1200	236.0	233.1	226.4	226.5	233.1	233.0	226.4	224.0
1250	245.3	241.0	233.9	233.5	240.4	242.0	233.3	232.2
1300	253.6	249.1	242.3	241.1	247.3	250.0	240.7	
1350	261.6	257.5	250.0	249.0	255.3	259.0	248.5	245.7
1400	269.2	265.2	258.0	255.7	263.9	266.0	256.2	254.5
1450	278.2	274.1	265.0	263.8	271.9		263.4	
1500	286.8	282.3	272.8	271.4	280.5	283.5	270.6	268.5
1550	293.8	289.7	280.3	278.8	288.5	291.9	278.8	276.2
1600	302.2	298.4	288.3	286.6	298.4	299.8	286.6	283.7
1650	310.4	307.4	294.9	294.0	307.7	308.1	294.0	291.0
1700	318.8	315.7	301.8	301.8	314.1	316.4	300.2	299.7
1750	327.0	324.1	308.4	309.8	321.7	325.4	307.2	306.9
1800	335.4	332.9	317.4	317.0	330.5	333.5	315.6	314.3
1850	343.4	341.3	323.5	324.5	338.5	343.4	322.8	320.9
1900	351.9	349.5	332.1	332.4				328.3
1950	359.2	358.5	339.6	339.5	355.3		338.0	335.6
2000	368.6	368.2	346.0	347.2	366.9	363.6	344.8	341.9
2050	376.8	376.3	354.7	353.4	376.7		350.0	350.3
2100	385.4	386.5	363.8	361.4	381.9	383.8	360.8	358.5
2150	393.4	395.9	370.8	369.7	388.9	393.7	368.5	365.9
2200	402.0	403.0	380.2	376.2	398.9		375.4	371.1
2250	410.2	408.5	386.0	386.4	405.5	407.7	381.5	376.9

SH-WAVE TIME-DISTANCE DATA

	(0°) 000 3D	(180°) 000 3R	(45°) 045 3D	(225°) 045 3R	(90°) 090 3D	(270°) 090 3R	(135°) 135 3D	(315°) 135 3R
<u>X</u>								
2150	393.8	395.3	371.6	369.7		392.6	368.1	366.1
2200	401.5	403.5	379.6	381.8		402.0	375.3	371.1
2250	410.4	411.9	385.9	386.6		408.7	382.0	379.5
2300	419.2	421.5	391.9	392.2		417.7	387.2	386.7
2350	427.4	427.9	398.4	398.0		425.1	393.4	
2400	435.6	434.7	408.0	406.6		434.5	400.7	401.3
2450	443.1		415.8	412.1		442.7	406.5	407.5
2500	451.7	453.3	422.5	418.9			418.3	
2550	459.7	462.5	430.4	425.1		455.9	424.9	426.1
2600	468.5	468.9	436.9	434.3		466.4	432.7	432.3
2650	476.0	478.7	446.1	441.1		474.3	436.8	438.5
2700	484.8	484.7	452.5	449.1		482.8	445.0	447.1
2750	491.6	493.9	458.9	457.2		493.0	451.9	454.3
2800	500.3	504.3		466.3		501.1	458.8	462.7
2850	509.2	514.5	473.8	472.8		511.0	469.1	468.7
2900	516.2	522.1		479.6			476.4	475.1
2950	525.8	529.5	487.9	485.5		526.9		485.5
3000	533.7	539.9	494.4	495.1		535.1	487.1	491.5
3050	542.2	546.5	500.7	500.5		541.6	494.4	496.9
3100	549.8	553.3	510.0	509.6		550.9		505.1
3150	558.8		518.1	516.8		559.8	512.5	513.5
3200	566.4	570.9		524.1			518.2	518.9
3250	576.4	578.3		530.8		575.0	525.4	527.1
3300	583.2	585.7		537.2			533.1	535.7

P-WAVE TIME-DISTANCE DATA

TABLE D-II

	(0°)	(180°)	(45°)	(225°)	(90°)	(270°)	(135°)	(315°)
	000	000	045	045	090	090	135	135
<u>X</u>	<u>1D</u>	<u>1R</u>	<u>1D</u>	<u>1R</u>	<u>1D</u>	<u>1R</u>	<u>1D</u>	<u>1R</u>
50	12.5	12.3	10.5	10.2	10.5	8.3	10.4	9.7
100	18.5	18.6	16.6	16.5	18.7	14.6	18.8	18.2
150	25.3	24.9	20.8	22.8	25.0	20.8	24.9	24.5
200	31.1	31.1	29.2	26.8	29.1	27.0	29.9	30.7
250	37.5	35.3	33.4	33.0	35.3	31.2	35.2	35.1
300	41.5	41.6	39.4	39.2	41.5	37.2	39.2	41.3
350	45.8	45.7	45.8	43.4	45.7	43.6	45.5	46.3
400	51.9	49.9	49.9	47.6	49.9	47.8	49.6	50.7
450	56.0	56.1	54.0	51.7	56.2	51.8	53.8	55.7
500	60.4	60.3	58.2	55.9	60.3	56.0	58.2	60.1
550	64.2	64.5	62.4	60.0	64.4	60.2	64.2	63.8
600	68.4		66.6		68.6	64.2	66.6	68.2
650	72.5	72.8		70.5	72.8	70.5	70.5	72.6
700	76.7	77.0	74.8	74.6	74.8	74.7	76.6	78.5
750	80.8	81.1	79.2	78.8	79.1	78.9	78.8	82.6
800	85.2	85.3	83.2	83.0	83.1	83.0	85.0	84.8
850	89.3	89.3	87.4	87.2	87.4	87.0	89.2	88.8
900	93.4	93.6	91.4	91.4	91.4	89.1	93.2	95.1
950	97.6	97.7	95.5	95.6	95.8	93.4	97.2	97.3
1000	101.7	101.8	99.7	99.8	99.8	97.6	101.6	101.6
1050	105.8	105.9	104.2	103.8	104.0	101.6	105.8	105.7
1100	110.0	110.0	108.2	108.0	108.2	105.8	108.0	109.5
1150	114.2	114.2	112.2	112.2	112.2	110.0	114.2	114.1
1200	118.2	118.3	116.2	116.4	116.4	114.2	118.2	118.2

P-WAVE TIME-DISTANCE DATA

	(0°)	(180°)	(45°)	(225°)	(90°)	(270°)	(135°)	(315°)
	000	000	045	045	090	090	135	135
<u>X</u>	<u>2D</u>	<u>2R</u>	<u>2D</u>	<u>2R</u>	<u>2D</u>	<u>2R</u>	<u>2D</u>	<u>2R</u>
1100		109.9	108.0	108.2	107.9	105.8	109.8	109.7
1150	114.1	114.1	112.2	112.4	112.1	110.1	113.7	114.3
1200	118.2	118.2	116.2	116.6	116.3	114.2	117.8	117.8
1250	122.4	120.3	120.3	120.8	120.5	118.2	122.1	122.2
1300	126.7	124.5	124.5	124.8	124.5	122.6	126.3	125.9
1350	130.8	128.6	128.6	129.0	128.6	126.6	130.4	130.2
1400	134.8	132.8	132.6	133.2	132.8	130.8	132.4	134.4
1450	139.0	136.9	137.0	137.4	137.0	135.0	136.6	138.6
1500	143.1	141.1	141.1	141.4	141.0	139.2	140.9	142.7
1550	147.1	143.3	145.3	145.6	145.2	143.3	144.9	147.0
1600	151.3	147.2	149.4	149.8	149.3	147.4	149.1	151.2
1650	153.5	151.6	153.5		153.4	151.6	153.3	155.1
1700	157.6	155.8		158.8	155.5	155.6	157.4	159.3
1750	161.7	159.9	161.8	162.2	159.7	159.8	161.5	165.6
1800	166.0	163.9		166.4	163.8	164.0	165.7	169.7
1850	169.9	168.0	170.2	170.6	168.0	166.2	169.9	173.9
1900	174.3	172.3	174.2	174.6	172.0	170.4	174.2	178.1
1950	178.6	176.4	178.4	178.8	176.2	174.4	178.2	182.0
2000	182.7	180.7	180.4	183.0	180.3	178.6	182.3	186.4
2050		184.8	184.5	187.2	182.4	182.8	186.5	190.4
2100	188.9	188.8	188.8	191.4	186.6	186.9	190.6	194.5
2150	192.9	193.2	194.0	195.6	190.8	191.2	194.7	198.7
2200	197.1	197.4	199.2	199.8	195.0	195.3	199.0	203.1
2250		201.5	203.4	204.0	199.2	199.6	203.1	207.2



P-WAVE TIME-DISTANCE DATA

	(0°)	(180°)	(45°)	(225°)	(90°)	(270°)	(135°)	(315°)
	000	000	045	045	090	090	135	135
<u>X</u>	<u>3D</u>	<u>3R</u>	<u>3D</u>	<u>3R</u>	<u>3D</u>	<u>3R</u>	<u>3D</u>	<u>3R</u>
2150		193.1	194.6	195.6	190.1	190.8	193.4	200.2
2200	197.1	197.3	198.9	199.9	194.3	195.0	197.5	202.3
2250	203.3	201.4	203.0	204.0	198.4	199.1	203.8	206.5
2300	207.5	203.5	205.2	208.2	202.4	203.1	207.8	210.7
2350	211.5	207.6	209.3	212.4	204.5	207.4	212.0	214.8
2400	215.8	211.8	215.4	216.5	210.8	211.8	214.0	219.0
2450	219.9	216.0	219.4	221.7	214.8	215.6	218.2	225.2
2500	222.0	220.1	223.4	224.9	219.1	219.7	221.2	227.3
2550	228.1	224.3	228.0	226.9	223.2	224.2	226.6	231.5
2600	230.1	228.5	232.0		227.3	228.2	230.7	235.5
2650	234.5	232.6	236.2	237.2	231.6	232.4	234.8	239.6
2700	238.6	236.7	238.4	241.4	235.6	236.4	239.0	243.9
2750	240.7	240.9		245.6	237.7	240.6	241.0	247.8
2800	244.9	243.0	246.5	251.8	242.0	244.8	245.1	252.1
2850	249.0	247.2	250.8	254.4	245.9	249.0	249.4	256.2
2900	253.1	251.2	254.8	258.2	250.2	253.2	255.6	260.4
2950	257.4	253.4	259.0	262.6		255.4	259.7	264.8
3000	261.3	257.5	265.4	266.4	258.4	259.6	263.8	268.8
3050	265.5	263.7	267.2	268.5	262.5	263.6	265.9	272.8
3100	269.6	267.8	269.4	272.8	266.7	267.8	271.0	277.2
3150	273.9	272.2	273.2	279.0	270.8	272.0	276.4	281.3
3200	279.1	276.3	277.6	283.1	274.9	276.4	280.5	283.3
3250	282.0	280.4	282.0	287.2	279.1	280.6	284.6	285.6
3300	286.3	284.6	288.0	291.6		284.6	288.8	289.6

## APPENDIX E

# APPENDIX E

## SEISMIC VELOCITIES AND WHB DEPTHS

TABLE E-I

<u>SH-000-D</u>		<u>SH-000-R</u>		<u>SH-090-D</u>		<u>SH-090-R</u>	
(Vms <sup>-1</sup> )	Z(m)	(Vms <sup>-1</sup> )	Z(m)	(Vms <sup>-1</sup> )	Z(m)	(Vms <sup>-1</sup> )	Z(m)
899.6	8.5	1001.3	9.3	906.1	7.9	908.2	7.8
1175.9	13.5	1398.2	15.2	1245.1	13.6	1217.3	13.2
1322.9	17.3	1492.7	17.7	1430.3	17.7	1431.0	17.9
1447.3	21.3	1634.3	21.8	1505.9	20.4	1495.6	20.2
1514.9	24.1	1661.9	23.3	1549.6	22.5	1595.0	24.1
1589.2	27.6	1742.7	27.0	1626.5	26.3	1638.7	26.3
1753.7	34.5	1753.9	27.9	1745.7	31.7	1680.3	28.8
1776.2	35.9	1763.9	29.1	1843.3	36.3	1711.4	31.1
1839.6	39.7	1783.5	31.1			1764.9	34.8
		1811.0	33.7			1824.9	38.9

<u>SH-045-D</u>		<u>SH-045-R</u>		<u>SH-135-D</u>		<u>SH-135-R</u>	
(Vms <sup>-1</sup> )	Z(m)	(Vms <sup>-1</sup> )	Z(m)	(Vms <sup>-1</sup> )	Z(m)	(Vms <sup>-1</sup> )	Z(m)
1010.0	9.1	1033.2	8.6	1024.9	8.8	1083.9	8.5
1224.1	13.1	1231.0	12.5	1322.9	13.7	1272.1	12.2
1349.9	16.5	1364.4	16.1	1433.7	16.7	1398.2	15.6
1468.9	20.4	1483.9	19.9	1483.9	18.7	1494.1	18.9
1511.9	22.5	1585.8	23.7	1542.5	21.5	1588.2	22.5
1577.6	25.8	1623.0	25.7	1600.8	24.6	1627.8	24.6
1657.4	30.0	1668.3	28.4	1658.8	27.9	1684.0	27.8
1711.6	33.2	1701.2	30.7	1690.2	30.2	1715.3	30.0
1738.7	35.2	1722.0	32.6	1733.5	33.3	1726.9	31.2
1751.7	36.5	1749.7	35.1	1764.4	35.9	1737.6	32.4
1770.0	38.5	1783.5	38.2	1800.0	40.0	1746.7	33.7
1796.1	41.2	1800.4	40.0	1819.7	41.0	1755.9	35.1
1820.8	43.9	1818.6	42.2	1828.8	42.1	1790.3	39.4
1858.5	47.9	1837.3	44.5	1851.0	44.9	1819.7	42.9
1875.7	50.0	1865.4	47.9	1883.4	48.7	1851.0	46.6
1902.6	53.3	1888.5	50.8	1911.0	52.0	1868.0	48.8
1929.1	56.6	1940.2	56.7	1947.6	56.3	1872.8	49.7
2029.4	66.7	2049.7	67.2	1958.0	58.9	1898.1	53.5
				1964.3	58.9	1963.3	61.5
				2002.0	64.2	2021.9	68.2
				2087.7	74.1	2058.6	72.5

SEISMIC VELOCITIES AND WHB DEPTHS

<u>P-000-D</u>		<u>P-000-R</u>		<u>P-090-D</u>		<u>P-090-R</u>	
(Vms <sup>-1</sup> )	Z(m)	(Vms <sup>-1</sup> )	Z(m)	(Vms <sup>-1</sup> )	Z(m)	(Vms <sup>-1</sup> )	Z(m)
1869.9	8.4	1938.9	8.8	1795.1	7.3	2137.4	5.9
2330.3	12.8	2305.6	12.6	2326.7	12.3	2442.3	9.2
2527.4	15.9	2544.2	16.1	2600.7	16.0	2561.3	11.4
2736.1	19.6	2919.5	21.6	2832.7	20.0	2801.5	15.8
3000.0	24.5	3544.8	29.8	3066.4	24.1	3011.9	20.0
3242.6	29.3	3678.4	32.4	3298.7	28.7	3195.0	24.0
3424.7	33.4			3699.9	36.0	3672.7	32.8
3674.5	38.9						

<u>P-045-D</u>		<u>P-045-R</u>		<u>P-135-D</u>		<u>P-135-R</u>	
(Vms <sup>-1</sup> )	Z(m)	(Vms <sup>-1</sup> )	Z(m)	(Vms <sup>-1</sup> )	Z(m)	(Vms <sup>-1</sup> )	Z(m)
1953.8	8.3	2082.0	8.7	1863.1	8.2	1836.1	6.2
2344.6	12.3	2434.5	12.3	2251.0	12.3	2211.9	10.3
2636.7	16.2	2650.4	15.4	2736.1	17.9	2454.1	13.9
2848.6	19.8	2908.4	19.7	3048.0	22.2	2673.7	17.9
3029.8	23.4	3091.3	23.2	3305.9	26.5	2925.1	22.6
3356.8	29.5	3228.8	26.4	3448.0	29.4	3175.0	27.6
3685.1	35.6	3658.4	34.7	3647.8	33.7	3655.3	36.2

## BIBLIOGRAPHY

## BIBLIOGRAPHY

- Bennett, H. F., An Investigation into Velocity Anisotropy Through Measurements of Ultrasonic Wave Velocities in Snow and Ice Cores from Greenland and Antarctica. University of Wisconsin, 1968. (unpublished Ph. D. thesis)
- Bennett, H. F., Measurements of Ultrasonic Wave Velocities in Ice Cores from Greenland and Antarctica. Corps of Engineers, U. S. Army, June 1972.
- Crampin, S., R. McGonigle, and D. Bamford, Estimating Crack Parameters from Observations of P-wave Velocity Anisotropy. *Geophysics*, Vol. 45, No. 3, 1980.
- Crary, A. P., E. S. Robinson, H. F. Bennett, and W. W. Boyd, Glaciological Studies of the Ross Ice Shelf, Antarctica, 1957-60, IGY Glaciological Report 6, Am. Geog. Soc., 1962.
- Crow, E. L., F. A. Davis, and M. W. Maxfield, Statistics Manual. Dover Pub. 1960.
- Dorrer, E., W. Hofmann, and W. Seufert, Geodetic Results of the Ross Ice Shelf Survey Expeditions, 1962-63 and 1965-66. *Jour. of Glaciology*, Vol. 8, No. 52, 1969.
- Embleton, C., and C. A. M. King, Glacial and Periglacial Geomorphology, Edward Arnold Ltd., 1968.
- Gow, A. J., Drill-Hole Measurements and Snow Studies at Byrd Station, Antarctica. Corps of Engineers, U. S. Army, Report 78, Jan. 1961.
- Grant, F. S., and G. F. West, Interpretation Theory in Applied Geophysics, McGraw-Hill, 1965.
- Kamb, W. B., The Glide Direction in Ice. *Jour. of Glaciology*, Vol. 3, No. 30, 1961.
- Kohnen, H., and C. H. Bentley, Seismic Refraction and Reflection Measurements at "Byrd" Station, Antarctica. *Jour. of Glaciology*, Vol. 12, No. 64, 1973.

- Love, A. E. H., A Treatise on the Mathematical Theory of Elasticity. Dover Pub., 1944.
- MacDonald, W. J. P., and T. Hatherton, Movement of the Ross Ice Shelf near Scott Base. Jour. of Glaciology, Vol. 3, No. 29, 1961.
- Musgrave, M. J. P., Crystal Acoustics. Holden-Day, Inc., Calif. 1970.
- Officier, C. B., Sound Transmission. McGraw-Hill Comp., New York, 1958.
- Paterson, W. S. B., The Physics of Glaciers. Pergamon Press, Ltd., 1969.
- Postma, G. W., Wave Propagation in a Stratified Medium. Geophysics, Vol. XX, No. 4, p. 780-806, 1955.
- Ragle, R. H., B. L. Hanson, A. Gow, and R. W. Patenaude, Deep Core Drilling in the Ross Ice Shelf, Little America V, Antarctica, Corps of Engineers, U. S. Army, Report 70, 1960.
- Rigsby, G. P., Study of Ice Fabrics, Thule Area, Greenland. Corps of Engineers, U. S. Army, Report 26, 1955.
- \_\_\_\_\_, Crystal Orientation in Glacier and in Experimentally Deformed Ice. Jour. of Glaciology, Vol. 3, No. 27, p. 589, 1960.
- Robin, G. de Q., Glaciology. III. Seismic Shooting and Related Investigations. Norwegian-British-Swedish Antarctic Expedition, 1949-52. Scientific Results Vol. 5, 1958.
- \_\_\_\_\_, Ice Shelves and Ice Flow. Nature, Vol. 253, p. 168, 1975.
- Shumskii, P. A., Principles of Structural Glaciology. Dover Pub., Inc., New York, 1964.
- Spencer, T. W., Refraction Along a Layer. Geophysics, Vol. XXX, No. 3, p. 369, 1963.
- Stuart, A. W. and C. Bull, Glaciological Observations on the Ross Ice Shelf near Scott Base, Antarctica. Jour. of Glaciology, Vol. 4, No. 34, p. 399, 1963.
- Taylor, L. D., Structure and Fabric on the Burroughs Glacier, South-East Alaska. Jour. of Glaciology, Vol. 4, No. 36, p. 731, 1963.

Telford, W. M., L. P. Geldart, R. E. Sheriff, D. A. Keys,  
Applied Geophysics. Cambridge Univ. Press, 1976.

Thiel, E., and N. A. Ostenso, Seismic Studies on Antarctic  
Ice Shelves. Geophysics, Vol. XXVI, No. 6, 1961.

Zumberge, J. H., M. Giovinetto, R. Kehle, and J. Reid,  
Deformation of the Ross Ice Shelf near the Bay of  
Whales, Antarctica. IGY Report No. 3, May, 1960.